Available online at www.sciencedirect.com

ScienceDirect

Underground Space 27 (2026) 362–385

www.keaipublishing.com/undsp

Research Paper

Migration and release characteristics of gases in excavation of a tunnel within magmatic rocks reservoir

Jilu Zhang [a,b], Xiaohan Zhou [a,b], Xinrong Liu [a,b,*], Lei Fang [a,b], Lojain Suliman [a,b], Guoliang Li [c]

[a] School of Civil Engineering, Chongqing University, Chongqing 400045, China
[b] National Joint Engineering Research Center of Geohazards Prevention in the Reservoir Areas (Chongqing), Chongqing 400045, China
[c] China Railway First Survey and Design Institute Group Co., Ltd., Xi'an 710043, China

Received 17 June 2025; received in revised form 17 November 2025; accepted 29 November 2025
Available online 3 February 2026

Abstract

The emission of hazardous gases from surrounding rocks is one of the major factors threatening the safety of deep underground engineering construction. In particular, for non-coal-bearing strata, increasing attention has been paid to identifying the types of hazardous gas reservoirs and predicting the gas release patterns from the surrounding rock. This study reveals the generation and occurrence mechanisms of hazardous gases within magmatic rock strata in the Qinghai–Tibet Plateau. Based on the characteristics of the gas reservoirs, a model test was conducted to analyze the deformation of the surrounding rock and the gas migration behavior during tunnel excavation. To represent the characteristics of low-porosity magmatic rock fracture reservoirs, a gas migration–release evolution model was developed based on the ideal gas law. The evolution of gas migration and release in the surrounding rock throughout the tunnel excavation process was investigated. Furthermore, the influence of borehole layout on the tunnel face on the gas release efficiency was examined. The results show that the long-term gas release process can be divided into three stages: stable release stage, gas replenishment stage, and residual gas release stage. Before the tunnel intersects the reservoir, the gas escape is primarily driven by pore seepage. After the tunnel enters the reservoir, the fracture gas velocity increases rapidly and then decreases gradually, with the escaping gas predominantly originating from the reservoir fractures. In addition, the installation of exhaust boreholes results in an "S-shaped" increase in the gas flow volume at the tunnel face as the borehole area increases. The gas release efficiency is maximized when the ratio of the fracture trace length to the exhaust borehole area (l/a) ranges between 0.064 and 0.096. These findings provide deeper insights into the gas migration and release characteristics of tunnel surrounding rocks in magmatic rock strata.

Keywords: Hazardous gases; Tunnel excavation; Magmatic rock; Gas migration characteristics; Exhaust borehole

1 Introduction

With the advancement of deep underground engineering, high geostress and complex geological structures have posed increasingly severe challenges to tunnel construction safety. Particularly in deep strata, the enhanced airtightness of rocks, coupled with high-pressure conditions, creates a more favorable environment for the formation and accumulation of hazardous gases, leading to their widespread presence (Ahmadi & Hekmat, 2021; Chen et al., 2025; Tang et al., 2024). Consequently, high-pressure gas outbursts from the surrounding rocks represent a major hazard encountered during deep underground construction. Because of their significantly diverse formation mechanisms and random distribution patterns, non-coal-bearing strata pose a greater threat to engineering safety (Czarny et al., 2021; Lu et al., 2025; He et al., 2023). Therefore,

* Corresponding author at: School of Civil Engineering, Chongqing University, Chongqing 400045, China.
E-mail address: liuxrong@cqu.edu.cn (X. Liu).
Peer review under the responsibility of Tongji University

https://doi.org/10.1016/j.undsp.2025.11.005
2467-9674/© 2026 Tongji University. Publishing Services by Elsevier B.V. on behalf of KeAi Communications Co. Ltd.
This is an open access article under the CC BY-NC-ND license (http://creativecommons.org/licenses/by-nc-nd/4.0/).

an in-depth research on the formation mechanisms and migration characteristics of hazardous gases in tunnel surrounding rocks in non-coal-bearing strata is of critical significance to ensure the safety of underground engineering projects.

Tunnel excavation induces stress redistribution in the surrounding rock, thereby altering its permeability and leading to changes in the gas seepage paths within the reservoirs. Gas seepage in the surrounding rock is influenced by numerous factors, such as gas storage patterns, stress conditions of the surrounding rock, spatial relationship between the tunnel and reservoir, and geological features of the surrounding rock (Kang et al., 2013; Sun et al., 2025; Zhao et al., 2025). At present, research on gas migration and release in surrounding rock primarily focuses on the mechanisms of coal seam methane seepage. Numerous scholars have investigated the mechanisms underlying the outburst characteristics, adsorption–desorption characteristics, and fluid–solid coupling mechanisms. Various theories have been proposed regarding methane outbursts under different modes, seepage models have been developed for porous media, and the patterns governing safety thickness variations in coal seams have been elucidated (Guo et al., 2018; Torno & Toraño, 2023; Watanabe et al., 2023). These findings serve as crucial references for understanding gas seepage characteristics within typical representative formations such as coal measures.

For non-coal measure strata, significant variations exist in the lithological properties, gas types, and gas occurrence modes. Systematic theories regarding gas migration mechanisms remain underdeveloped (Cui et al., 2022; Zhu et al., 2007). Qiu et al. (2025) explored hazardous gas–geological structure interactions in southwest China, identified three gas generation pathways (hydrocarbon generation, thermochemical reactions, and hydrothermal migration), and proposed a risk prediction framework for tunnel gas hazards. Feng et al. (2023) conducted fluid–solid coupling simulations to analyze the damage in parallel tunnels caused by shallow gas-bearing strata near the Nakdong River (Republic of Korea) to elucidate the failure mechanisms linked to gas migration. Focusing on the Yuelongmen Tunnel (Chengdu–Lanzhou Railway), Luo et al. (2022) demonstrated that porous media seepage remains largely unaffected by blasting, whereas post blasting gas releases through fractured media intensify at pressures of more than 25 MPa. Current studies predominantly focus on specific engineering cases without in-depth investigations of the gas migration–release characteristics across different reservoir properties (Chen et al., 2020; Liu et al., 2006; Zhou et al., 2016). In particular, for magmatic rock strata, where hazardous gases mainly occur in fractured media, excavation-induced fracture aperture changes significantly, which affects the seepage behavior. Unlike coalbed methane, these gas reservoirs lack replenishment sources during release, resulting in distinct pressure evolution patterns. Existing research has yet to comprehensively examine the gas migration–release characteristics throughout the entire tunnel excavation process.

Moreover, methods such as ventilation, grouting, sealing, and borehole drainage have been widely adopted in engineering practice for the treatment of hazardous gases in tunnels (Cheng et al., 2018; Fang et al., 2019; Gao et al., 2023; Zhu & Cai, 2020). However, treatment measures for hazardous gases in non-coal measure strata need to be optimized based on the reservoir characteristics and surrounding rock properties. Field evidence has demonstrated that borehole drainage significantly enhances gas release in magmatic rock strata; however, the design principles for borehole arrangements in such reservoirs remain unclear. The current research fails to provide robust support for designing effective hazardous gas treatment strategies for magmatic rock formations.

In this study, the mechanisms of the formation and storage of hazardous gases in magmatic rocks were revealed by analyzing the regional geological structures. On this basis, a test platform was developed for the hazardous gas migration–release model in tunnel surrounding rock, and the migration patterns of these gases in the surrounding rock during the tunnel excavation process were analyzed. Furthermore, considering the effects of time, a computational model was established for the entire deformation–damage–seepage process. The gas release mechanism under the influence of tunnel excavation was clarified through numerical simulations, and an optimization scheme for the gas exhaust boreholes at the tunnel face was proposed. The research results provide a significant reference for the prediction and mitigation of hazardous gases in surrounding rocks of magmatic rock stratum tunnels.

2 Engineering background and equipment development

2.1 Geological engineering background

Figure 1 shows the geological information of the tunnel and gas release situation. The tunnel is situated at the southeastern edge of the Tibetan Plateau, where the regional tectonic activity is intense. The Xianshui River, Longmen Mountain, and Anning River fault zones are densely distributed around the tunnel site. Because of frequent tectonic activities, numerous intrusive rocks from different periods are distributed within the plate. The main rock type in the strata of the tunnel area is Miocene intrusive rock, which is a Cenozoic Tertiary magmatic rock.

During tunnel excavation at the working face of section DK234+109.5, a significant high-pressure gas outburst was encountered. The estimates indicate a gas reserve of approximately 5×10^5 m^3. Gas composition analysis revealed CO_2 (94%) as the primary component, with minor concentrations of CO (1%), O_2 (0.8%), and N_2 (4.2%). The main gas release zone was identified at the upper right section of the tunnel. After discovering the hazardous gases

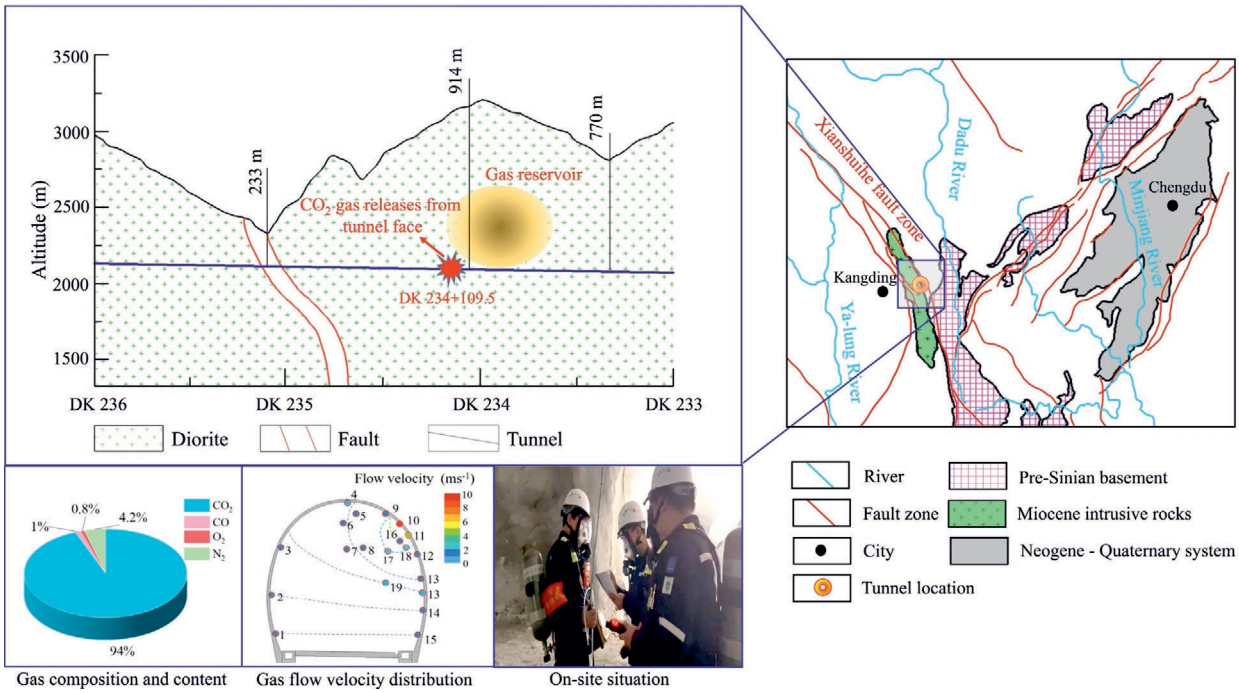

Fig. 1. Geological information of the tunnel and gas release situation.

escaping from the tunnel face, the engineers adopted drilling to increase the gas release efficiency. A total of 20 vent holes were drilled, with a diameter of 10 cm and a drilling depth of 10 m. The tunnel in the CO_2 emission zone has a burial depth of about 900 m, a tunnel height of 6.5 m, and a width of 6.8 m. The tunnel surrounding rock is predominantly tonalite. The rocks behind the excavation direction are relatively intact and are classified as Grade III surrounding rocks. Advanced geological exploration revealed that the rocks ahead of the excavation are mainly Grade IV–V, with no water in the fractures.

2.2 Generation and storage mechanism of hazardous gases in magmatic rocks

Current research on the source of hazardous gases in magmatic rocks suggests that the gas is produced by degassing during the condensation process of deep mantle magma intrusion (Goff & Janik, 2002; Stefánsson, 2017). The main types of hazardous gases are CO_2, CO, H_2S, and SO_2. The gas content increases with younger intrusion age, as older rocks experience gradual gas dissipation through pores and tectonic disturbances. Cenozoic magmatic rocks exhibit the highest gas reservoir potential because of their limited gas escape and structural stability. Meanwhile, the tunnel area is characterized by strong compression between the tectonic plates of the Qinghai–Tibet Plateau, resulting in a predominance of horizontal compressive stresses within the strata. The combined effect of the two aforementioned factors creates conditions for the generation and storage of hazardous gases in magmatic rocks. The specific process is as follows: magma intrusion → magmatic condensation with volume contraction to generate fractures and release gases → gas accumulation in the fracture-developed zones → formation of magmatic gas pockets → reduction of fracture space due to tectonic compression of the formation → increase in gas occurrence pressure to form high-pressure reservoirs. Figure 2 illustrates the formation process of high-pressure air sacs in magmatic rocks.

2.3 Development of a model testing system for gas migration and release in the surrounding rock

To analyze the characteristics of gas migration in the surrounding rock during tunnel excavation under constant reserve conditions, a tunnel model testing system was developed for gas migration and release in the surrounding rock. The model testing system primarily consists of a loading system, model test chamber, gas reservoir model, deformation monitoring platform, and data acquisition system, as illustrated in Fig. 3.

The model loading system can apply a maximum vertical stress of 1000 kN with a loading stroke of 0–20 cm. The model test chamber has dimensions of 1.5 m × 1 m × 1 m and can withstand a maximum loading pressure of 1 MPa. To ensure the sealing of the model test chamber, a 5-cm silicone pad was installed on the inner side of the upper cover plate. When the cover plate is compressed, the silicone pad undergoes lateral deformation, sealing the top of the model test chamber. The gas reservoir model can store 2.4 m^3 of gas, and the device can withstand a maximum gas pressure of 0.5 MPa. In addition, the deformation monitoring platform is equipped with a set of high-precision guide rail

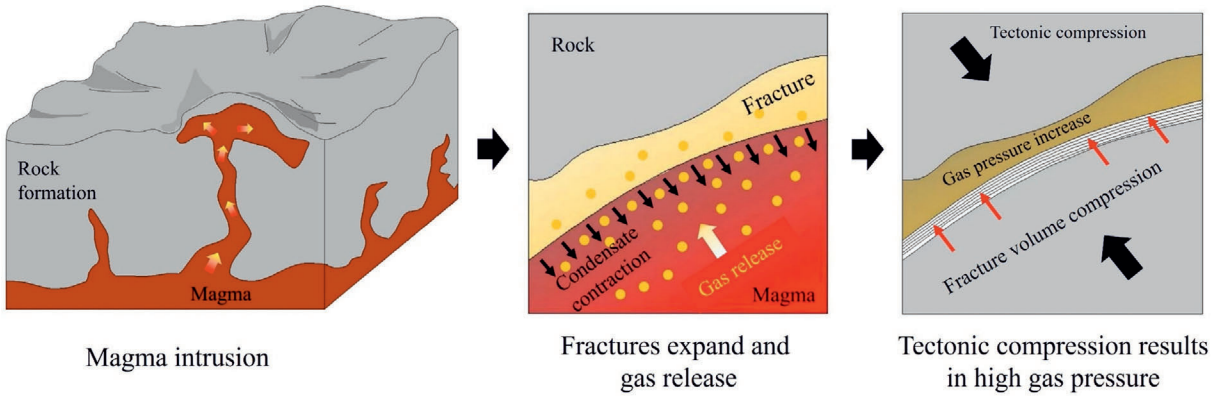

Fig. 2. Formation process of hazardous gas reservoirs in magmatic rocks.

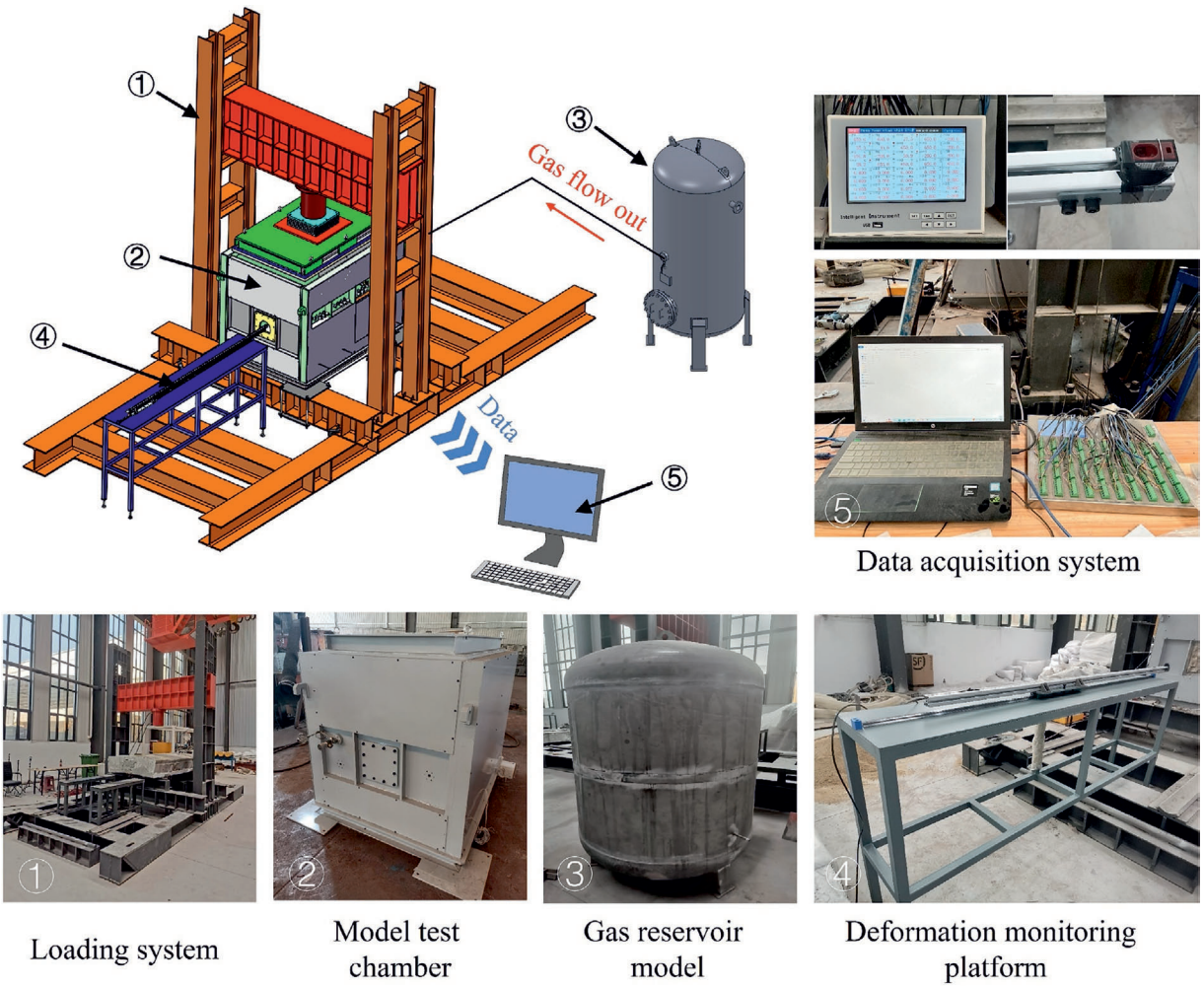

Fig. 3. Schematic and photographs of the model testing system.

laser rangefinders. The model test chamber has 13 gas pressure-monitoring sensors and 35 stress-monitoring sensors, whereas the gas reservoir model features a flow-monitoring sensor. This comprehensive setup enables an in-depth analysis of the surrounding rock deformation and gas migration characteristics during tunnel excavation.

2.4 Similarity theory of the model test

Based on similarity theory, the tunnel excavation model test under fluid–solid coupling should satisfy the following similarity relationships: (1) geometric similarity, (2) similarity in the physical and mechanical parameters of the

material, (3) similarity in stress state, and (4) similarity in time. The relationships between the various parameters of the model and on-site conditions are expressed as follows (Sun et al., 2023):

$$C_{\mathrm{L}} = \frac{L_{\mathrm{p}}}{L_{\mathrm{m}}}, \tag{1}$$

$$C_{\sigma} = C_{\mathrm{c}} = C_{\mathrm{Rt}} = C_{\mathrm{E}}, \tag{2}$$

$$C_{\sigma} = C_{\gamma} C_{\mathrm{L}}, \tag{3}$$

$$C_{\mathrm{K}} = \sqrt{C_{\mathrm{L}}}/C_{\gamma}, \tag{4}$$

$$C_{\mathrm{t}} = \sqrt{C_{\mathrm{L}}}, \tag{5}$$

where L_{p} and L_{m} represent the lengths of the prototype and the model, respectively; C_{σ}, C_{c}, C_{Rt}, C_{E}, C_{γ}, C_{L}, C_{K}, and C_{t} are the similarity ratios for stress, compressive strength, tensile strength, elastic modulus, weight, geometry, permeability, and time, respectively.

The in-situ tunnel surrounding rock consists of granite. The fundamental physical and mechanical parameters of the rock mass were obtained from uniaxial compression tests, Brazilian splitting tests, and permeability tests, as illustrated in Fig. 4. The tunnel has a height of 6.5 m and a width of 6.8 m, with an advancing rate of 5 m/day. Based on equipment parameters, on-site tunnel design, and mechanical parameters of the surrounding rock, a similarity ratio of 50 was chosen, resulting in $C_{\mathrm{L}} = C_{\sigma} = C_{\mathrm{c}} = C_{\mathrm{Rt}} = C_{\mathrm{E}} = 50$, $C_{\gamma} = 1$, and $C_{\mathrm{K}} = C_{\mathrm{t}} = 7$. In the model test, the single excavation length was 10 cm, and the tunnel height and width were 13 and 13.6 cm, respectively. The determination of the similarity ratio for the model test was primarily based on two aspects: the dimensions of the testing equipment and the strength of the model materials. With this similarity ratio, the distance between the tunnel and the model boundary exceeded four times the tunnel diameter, satisfying Saint–Venant's principle. Furthermore, the material strength under this scaling ratio fell within the conventional strength range of common materials.

Through multiple tests, the material mass ratio of the tunnel surrounding rock was determined as follows: sand :barite powder:iron powder:gypsum:cement: water = 35:20:5:20:5:15. Here, sand, iron powder, and barite powder served as aggregates, gypsum and cement as binders, and water as a mixing agent. The comparison results of the physical and mechanical parameters between the on-site surrounding rock and similar materials are shown in Table 1. Although there was a significant difference between the permeability parameters of the similar materials and the design parameters, the gas in the surrounding rock mainly flowed through the fractures during the model test. The seepage through the rock matrix can be considered to have no significant impact on the experimental results (Zhang et al., 2025; Ishibashi et al., 2023). Overall, the relevant parameters obtained from the similar materials satisfied the similarity design requirements. The similarity ratio of the rock mass elastic modulus in the table was slightly higher than that in the experimental design. Extensive studies (Shahin et al., 2016; Xu et al., 2019) have demonstrated that it is challenging for similar materials to maintain satisfactory similarity across all parameters. Therefore, the configuration of the experimental materials was primarily focused on testing the key similarity parameters. Since the failure of the surrounding rock is predominantly controlled by the rock mass strength, the similarity of the rock mass strength was mainly considered in the model test.

Additionally, since the fracture aperture of the reservoir within the in-situ tunnel surrounding rock cannot be directly measured, a review of existing literature indicates that reservoir fracture apertures typically range from 1×10^{-3} to 1×10^{-5} m (Fang et al., 2025; Zhang et al., 2023). In this study, a fracture aperture of 1×10^{-4} m was adopted, corresponding to a permeability of approximately 1×10^{-9} m^2. Subsequent gas flow monitoring in the model test revealed that when the reservoir was excavated to a depth of 1 m, the measured flow rate was 0.7 L/min, and the fracture exposure length was approximately 0.6 m at the working face. Based on calculations, the permeability of the rock fractures in the reservoir was estimated to be 4×10^{-10} m^2, yielding a similarity ratio

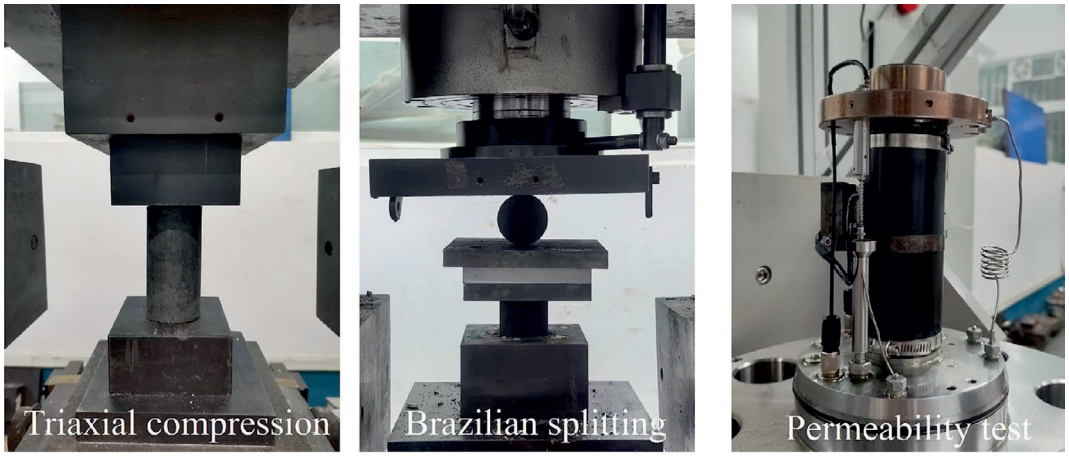

Fig. 4. Fundamental physical and mechanical parameter tests of the rock mass.

Table 1
Comparison of physical and mechanical parameters between on-site surrounding rock and tunnel surrounding rock in the model test.

Content	Density (kg/m^3)	Uniaxial compressive strength (MPa)	Uniaxial tensile strength (MPa)	Elastic modulus (GPa)	Permeability (m^2)
Prototype	2.7×10^3	144	5.6	25.5	1.5×10^{-19}
Model	2.3×10^3	2.98	0.13	0.27	3.46×10^{-16}
Similarity ratio	1.17	48.32	43.08	94.4	4.3×10^{-3}

of 2.5. Overall, the fracture permeability of the model effectively represents the seepage behavior of the in-situ surrounding rock. Moreover, the model's fracture permeability was significantly higher than that of the rock-simulating material, which aligned with the gas migration mechanism in magmatic reservoirs, where fractures serve as the primary pathways.

Regarding the similarity of the rock joint, based on the on-site construction results, the surrounding rock joint had no significant impact on gas seepage before the tunnel exposed the reservoir. The rock layers were closely combined, and the crack openings were extremely small. The model test could not fully reproduce the bedding characteristics, so the layered filling method was adopted to represent the bedding.

2.5 Model test procedure

The model simulated the fracture effects on gas migration during tunnel excavation by incorporating two components: (1) intact Grade III surrounding rock with interlayer fractures simulated via layered filling and (2) gas reservoir fractures constructed from prefabricated blocks (dimensions: 20 mm × 100 mm × 1000 mm) assembled with cementitious gap fillers. The reservoir fracture occupied a 750 mm radius quarter-circle on the right side of the model, with both bedding planes and fracture dip angles of 45°.

Five monitoring sections (S1–S5) were established to track the rock deformation and gas migration during tunnel excavation. S1–S4 each had 4 vertical earth pressure sensors, 3 lateral earth pressure sensors, and 3 gas pressure sensors, whereas for S5, the gas sensors were replaced with 1 gas sensor. The locations of the sensors for the model test is shown in Fig. 5. The sensor layouts included (1) vertical sensors placed 2 cm below the tunnel base and installed 2, 5, and 10 cm above the vault, (2) lateral sensors placed 2, 5, and 10 cm from the haunch, and (3) gas sensors installed along the fracture dip at 2, 6.5, 14 cm vertical intervals.

The on-site tunnel has a burial depth of around 900 m, with a corresponding self-weight stress of approximately 25 MPa. Based on similarity relations, the applied test load was 0.5 MPa. Current results indicate that the occurrence pressures of CO_2 reservoir gases predominantly fall within the range of 0–3 MPa (Huo et al., 2021; Yuan et al., 2022). Therefore, 3 MPa was selected as the representative gas pressure in this study, with a corresponding loading pressure of 0.06 MPa applied in the model test. The model test was divided into two parts. The first part involved simulating the tunnel excavation process, with each excavation advancing 10 cm at a time. Each excavation cycle in the model test took 3.5 h, and there were a total of 12 excavations. The second part involved simulating the gas release process, where the gas was continuously released after the tunnel excavation was complete until the gas pressure inside the gas reservoir reached a value of 0. Figure 6 illustrates the model test procedure.

3 Analysis of model test results

3.1 Stress–deformation characteristics of the surrounding rock during tunnel excavation

Because the deformation value of the tunnel vault obtained by the laser rangefinder is the relative deformation calculated from two excavation monitoring sessions, the relative displacement generated by the last excavation section (12th excavation) cannot be obtained. Figure 7 shows the evolution curves of the tunnel vault settlement during the excavation process. When the tunnel face remains outside the reservoir fracture zone, the vault deformation initially settles rapidly before stabilizing nearly constantly as the excavation progresses, reaching near-complete stability when the excavation distance exceeds twice the tunnel diameter, with the vault settlement accounting for over 90% of the total settlement. As the tunnel face approaches the reservoir, subsequent construction activities increasingly influence the vault settlement. When the excavation distance reaches 900 mm (contacting the fractured reservoir), the excavation-induced deformation contributes to approximately 73% of the total deformation. Analysis of the vault deformation versus the excavation distance reveals that the settlement intensifies as the tunnel face nears the fractured reservoir, the settlement peaks at the reservoir contact, and then slightly decreases thereafter. This pattern primarily results from the high in-situ stress at the interface between the fractured reservoir and intact surrounding rock, where combined effects of elevated unloading and fracture deformation induce greater deformation.

Figures 8 and 9 show the evolution curves of vertical and horizontal stresses in the surrounding rock during tunnel excavation, respectively. Both vertical and horizontal stresses exhibit a stepped variation with excavation. The

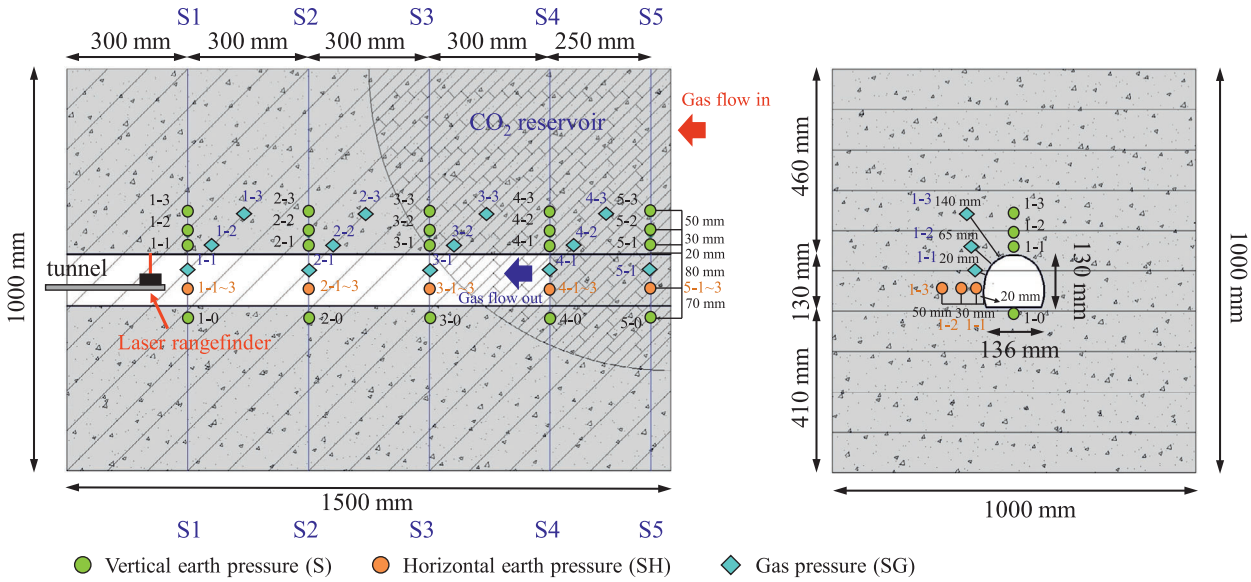

Fig. 5. Locations of the sensors for the model test.

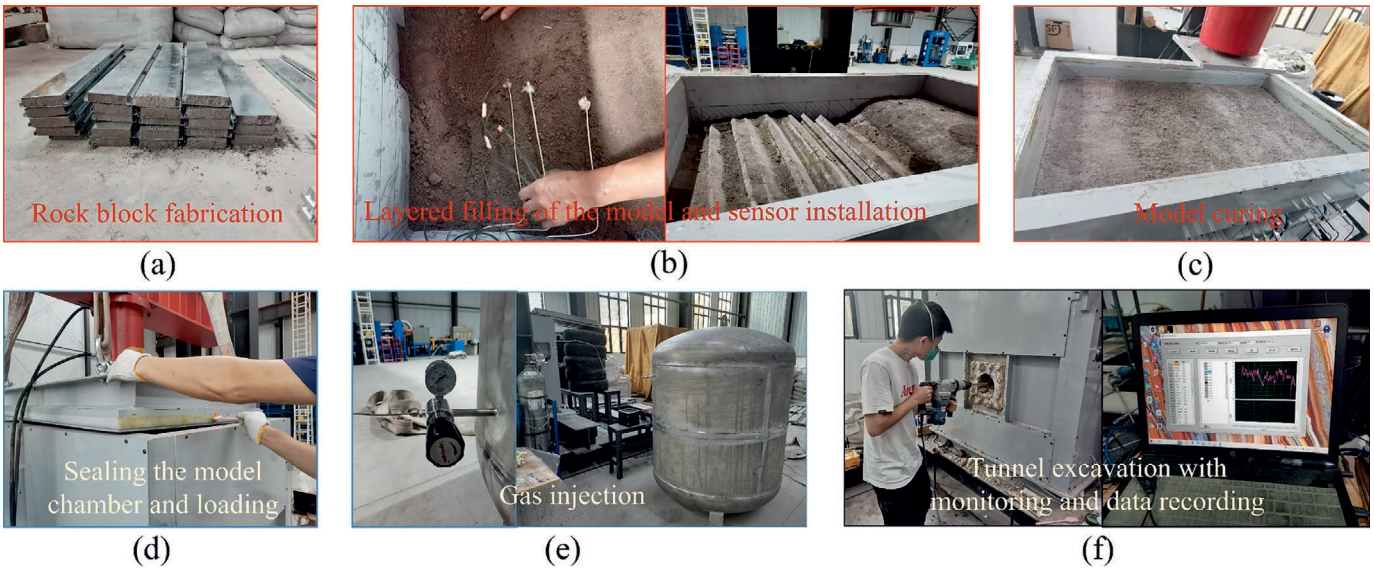

Fig. 6. Model test procedure.

vertical stresses at the vault and tunnel bottom of the surrounding rock decrease with excavation, and the stress attenuation amplitude decreases with increasing radial distance from the measurement point. The stress release ratio is mathematically expressed as the ratio of the stress variation amplitude during each phase to the initial stress, as given by Eq. (6). Comparative analysis of monitoring sections reveals that the vertical stress release in surrounding rocks diminishes as the tunnel face approaches the fractured reservoir. Using vault monitoring point 1 of each section as an example, the amounts of stress release after the excavation of monitoring sections S1, S2, S3, S4, and S5 are 39%, 40%, 30%, 30%, and 12%, respectively, where the lower rate for S5 is attributed to its unexcavated status at measurement. Further stress evolution analysis shows that within the intact surrounding rock, vertical stress release primarily occurs within approximately 0.8 times the tunnel diameter before and after excavation, accounting for 35%–80% of the total release, where this proportion decreases as the tunnel face nears the fractured reservoir. Upon entering the fractured reservoir, the unloading zone expands due to the lower strength of the surrounding rock, causing significant vertical stress reductions at S4 and S5 prior to the tunnel face arrival. The excavation-induced stress release in these sections contributes about 12% of the total release. Moreover, the process of gas release further reduces the vertical stress in the surrounding rock, and the stress release proportions at S1, S2, S3, S4, and S5 are 1.5%, 1.4%, 5.2%, 4.6%, and 1.5%, respectively, during the gas release stage.

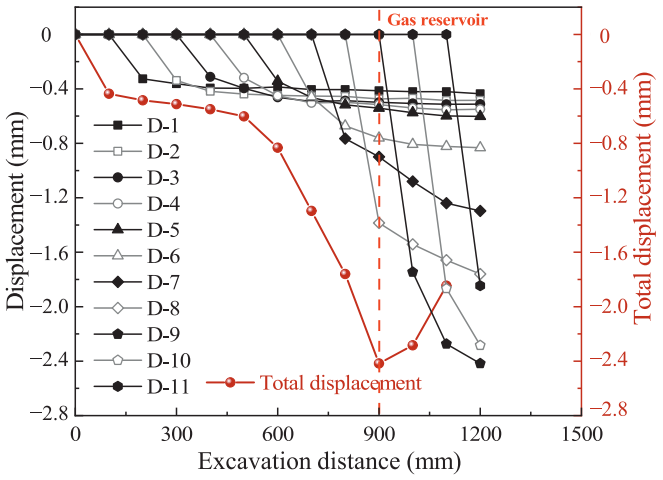

Fig. 7. Evolution curves of the tunnel vault settlement during the excavation process.

$$\alpha = \begin{cases} \frac{\sigma_0 - \sigma_e}{\sigma_0} & \text{Excavation} \\ \frac{\sigma_e - \sigma_r}{\sigma_0} & \text{Gas-release} \end{cases}, \quad (6)$$

where α is the stress release ratio, σ_0 is the initial stress, σ_e is the stress after excavation, and σ_r is the stress after gas release.

The horizontal stress at the tunnel haunch first increases and then slightly decreases with excavation, indicating that the haunch is subjected to a more pronounced lateral compression after deep tunnel excavation. Taking monitoring point 1 of each monitoring section as an example, when the tunnel is within intact surrounding rock, the increase in horizontal stress at the haunch mainly occurs within approximately ±0.8 times the tunnel diameter from the monitoring section, which is consistent with the vertical stress pattern. Once the tunnel enters the fractured reservoir, the horizontal stress increases significantly during excavation, and the increase becomes more pronounced the closer the tunnel face is to the monitoring point. In addition, the gas release from the fractured reservoir leads to a certain reduction in the horizontal stress. Compared with the initial state, the stress reduction caused by the gas release ranges from approximately 2.4% to 8.3%, and the closer the tunnel face is to the reservoir, the greater the reduction.

3.2 Gas migration characteristics of the surrounding rock during tunnel excavation

Figure 10 shows the gas pressure evolution curves of the surrounding rock. Monitoring sections S1 and S2, outside the fractured reservoir, maintained a zero gas pressure throughout the test. S3, at the intact rock–reservoir interface, contains measurement point SG3-1 in the intact rock

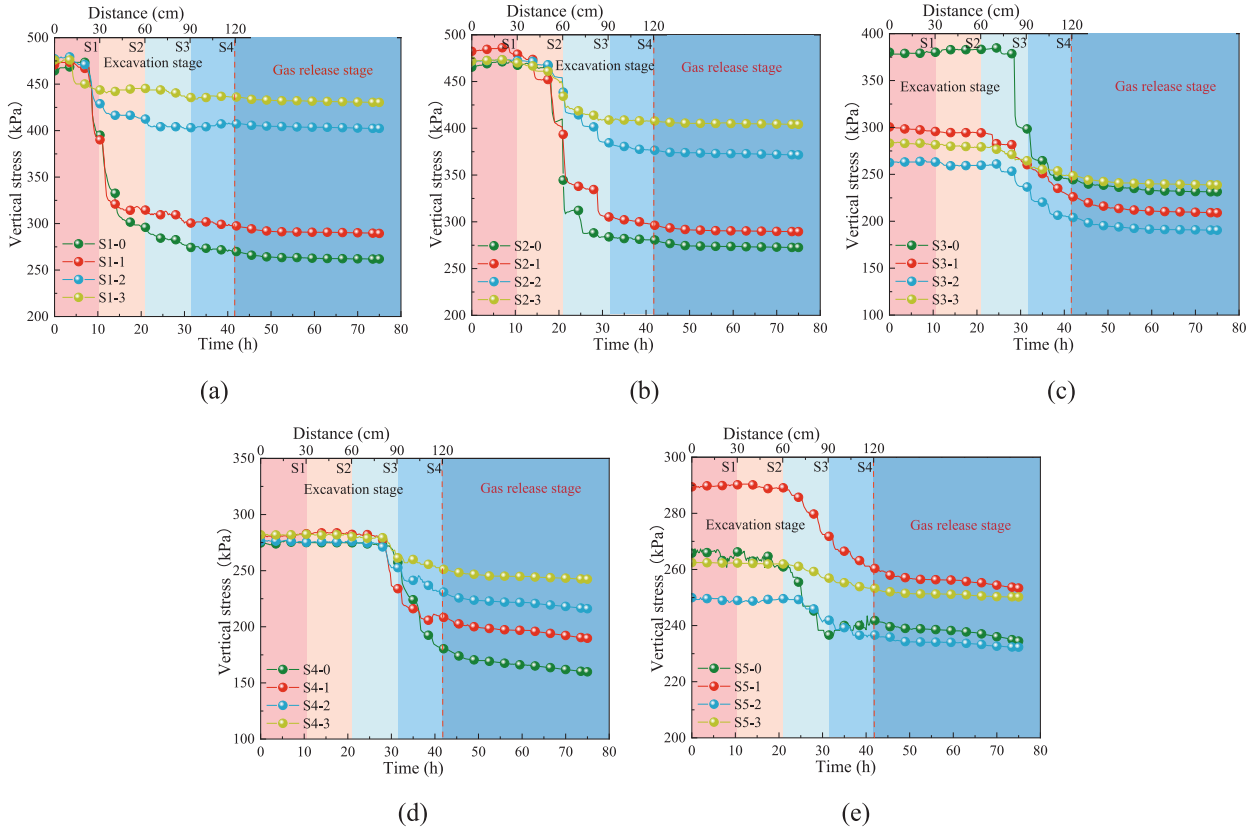

Fig. 8. Vertical stress evolution curves of the surrounding rock. (a) S1, (b) S2, (c) S3, (d) S4, and (e) S5.

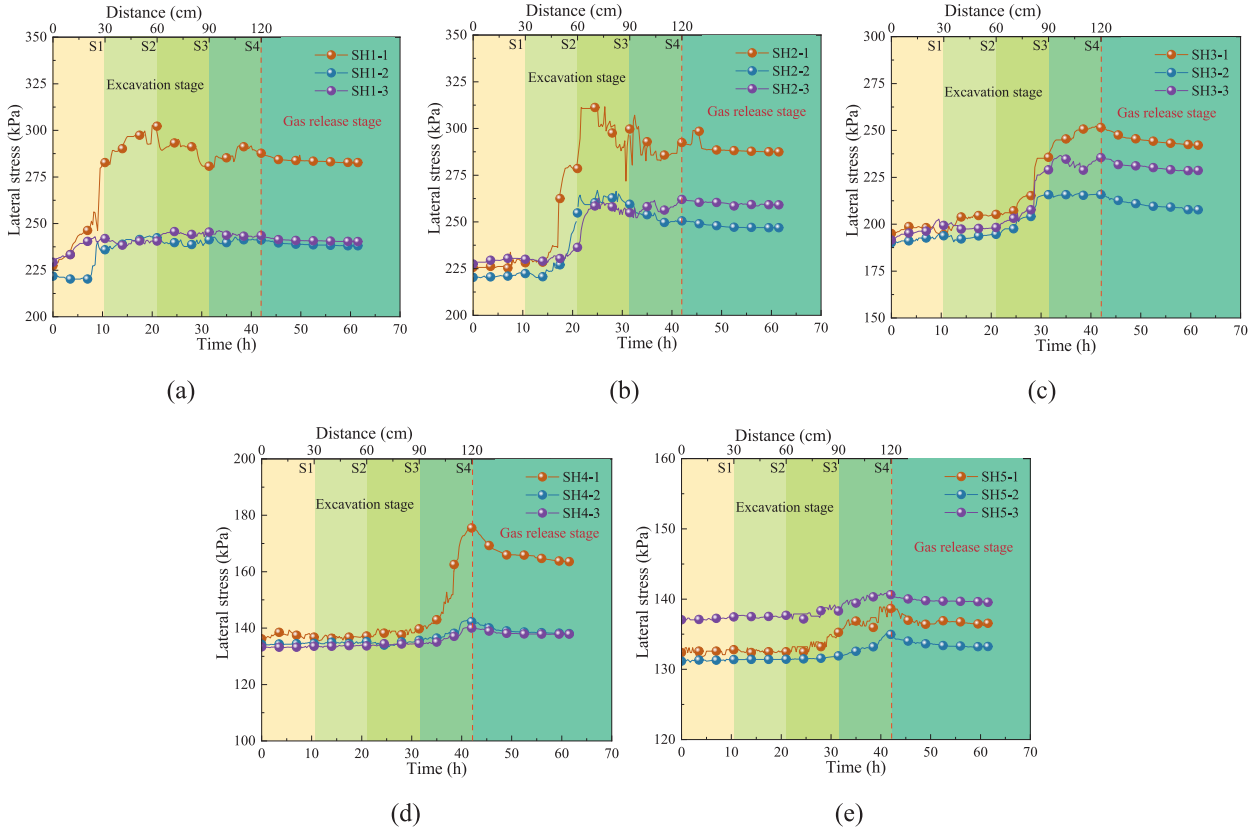

Fig. 9. Horizontal stress evolution curves of the surrounding rock. (a) S1, (b) S2, (c) S3, (d) S4, and (e) S5.

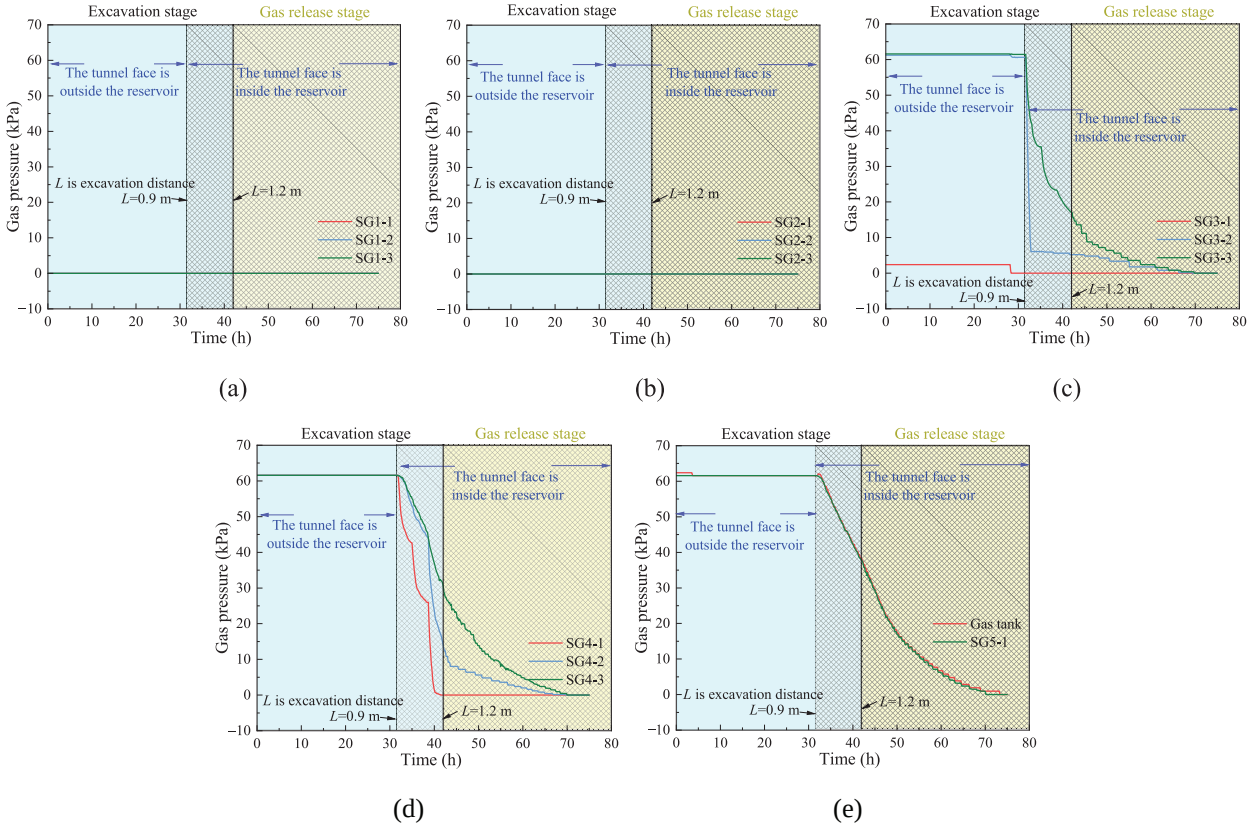

Fig. 10. Gas pressure evolution curves of the surrounding rock. (a) S1, (b) S2, (c) S3, (d) S4, and (e) S5.

and SG3-2/SG3-3 in the reservoir. S4 and S5 are fully within the fractured reservoir.

During tunnel excavation (0–42 h), the gas pressure within the reservoir remains stable until the tunnel face intersects it, indicating that the high-strength, low-permeability reservoir possesses good sealing capacity. Before entering the fractured reservoir, the intact surrounding rock between the tunnel face and reservoir limits the changes in the excavation-induced gas pressure. Upon entering the fractured reservoir, the gas pressure drops sharply and continues to decrease nonlinearly in a stepwise manner as the excavation progresses, although the rate of pressure reduction diminishes with an increase in the excavation distance. Further comparison of the gas pressure evolution curves at monitoring sections S3 and S4 within the reservoir reveals that, when the tunnel is located at the reservoir boundary, the surrounding rock experiences a greater gas pressure drop compared with that within the far end of the reservoir (gas tank). This is attributed to the poorer fracture connectivity at the boundary and the greater distance from the gas supply source. For example, when the excavation distance reaches 120 cm, the gas pressures at SG3-3 and SG4-3 decrease by approximately 72.3% and 50.1%, respectively, whereas the pressure at the far end of the reservoir (gas tank) decreases by approximately 37.7%.

During the gas release stage (42–75 h), the gas pressures at different locations within the reservoir exhibit a nonlinear decreasing trend: the gas pressure initially decreases rapidly, followed by a gradual decline over time. Moreover, the slopes of the pressure evolution curves during the gas release stage are generally lower than those during tunnel excavation. This is mainly because the pressure variation during excavation is positively correlated with the exposed area of the reservoir, and the initial gas pressure in the reservoir is relatively high, resulting in a larger pressure drop.

To analyze the radial gas pressure variations in the surrounding rock during tunnel excavation and gas release, sections S3 and S4 were selected for analysis (Figs. 11 and 12). During tunnel excavation, the gas pressure release rate decreases radially, with location-dependent variations. At the reservoir edge (S3), the gas pressure drops by approximately 90% within $0.5d$ (where d is the tunnel height) when the excavation distance reaches 1 m (i.e., the tunnel face contacts the reservoir). Beyond a radial distance of approximately $1.1d$, the gas pressure decreases by about 42%, and only a mere 11% decrease occurs at the far end of the reservoir, indicating that the primary release zone is within $0.5d$. Beyond this, the release rates decline, but remain higher than at the far end of the reservoir. As the tunnel excavation length L increases, the degree of gas pressure release in S3 also increases, with more pronounced variations observed at farther radial distances. When the excavation distance reaches 1.2 m, the release rate decreases linearly, and the changes in the surrounding rock pressure exceed those at the far end of the reservoir.

When the monitoring section was within the reservoir (S4), the gas pressure drops immediately once the tunnel enters the reservoir, with variations primarily confined to $0.15d$. As the radial distance increases, the pressure release rate in the surrounding rock converges with that at the far end of the reservoir. When the tunnel reaches the monitoring section ($L = 1.2$ m), the release rate reaches its peak and decreased linearly with the radial distance. These findings indicate that the gas pressure release near the tunnel face exceeds that in the distal reservoir during tunnel excavation, suggesting that, under short release periods, the gas expelled from the surrounding rock surpasses replenishment from the far end of the reservoir, with pressure variations primarily governed by the initial gas content near the tunnel.

Analysis of the radial gas pressure evolution curves in the surrounding rock during the gas release stage shows that the pressure release rate decreases approximately linearly with increasing radial distance. As the release time extends, the curve variations gradually reduce, and the release rate approaches that at the far end of the reservoir. This indicates that, in the long-term release phase, the gas pressure distribution in the surrounding rock is primarily governed by gas replenishment from distant regions and controlled by the fracture network of the reservoir.

Figure 13 shows the evolution curves of the gas flow velocity and accumulated flow volume at the far end of the reservoir during the entire tunnel excavation process. The total amount of released gas exhibits an inverted "S-shaped" variation with increasing time. The gas flow velocity shows different characteristics in the tunnel excavation and gas release stages. In the tunnel excavation stage, the gas velocity suddenly increases when the tunnel face contacts the gas reservoir, and it increases linearly with the excavation distance within the gas reservoir. This is primarily due to the increasing seepage area of the surrounding rock as the excavation progresses. During the release stage, the gas velocity initially decreases slowly, then rapidly, and finally slows down again.

The relationship between the slope of the flow rate curve and time is plotted in Fig. 14 to analyze the evolution patterns of the gas flow rates at different time intervals. During the initial gas release stage, the slope of the curve exhibits no significant variations with time. As time progresses, the slope decreases substantially before stabilizing again. Notably, as the gas release approaches completion, the slope of the curve rebounds. Based on the evolution of the slope of the flow rate curve, the gas release evolution can be divided into three stages. (1) Stable release stage of the reservoir, where there are no significant variations in the slope. The overflow of gas in the tunnel is mainly supplied by the reservoir gas near the surrounding rock, and the pressure changes in the distal reservoir are relatively lagging, resulting in minimal velocity changes during this stage. (2) Gas replenishment stage of the reservoir, where there is a sharp decrease, followed by stabilization of the slope. This stage is characterized by a decrease in

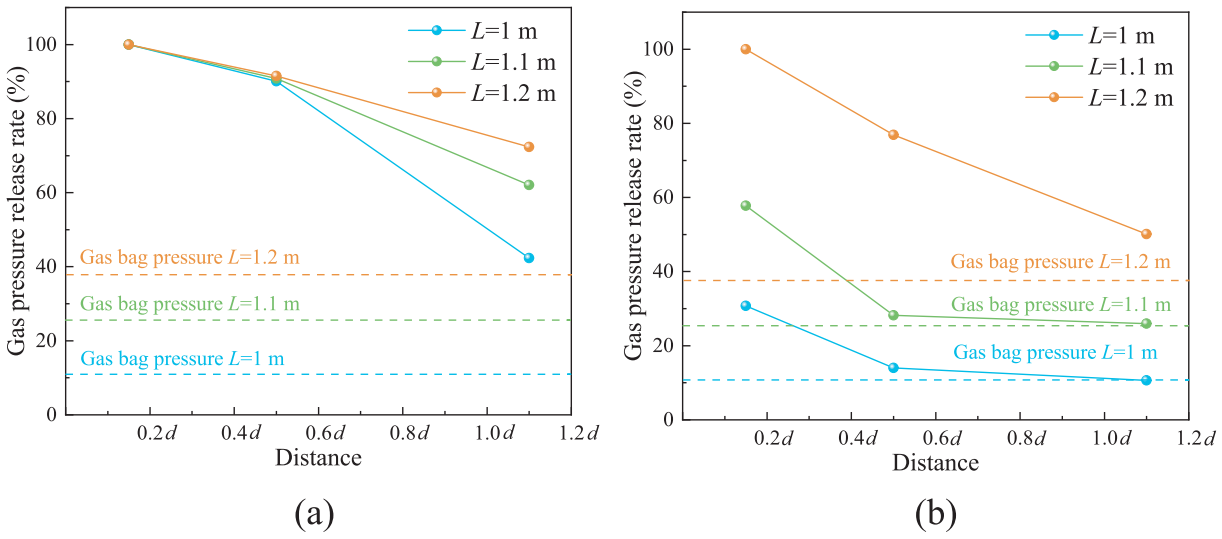

Fig. 11. Radial gas pressure evolution curves of the surrounding rock during the excavation stage. (a) S3, and (b) S4.

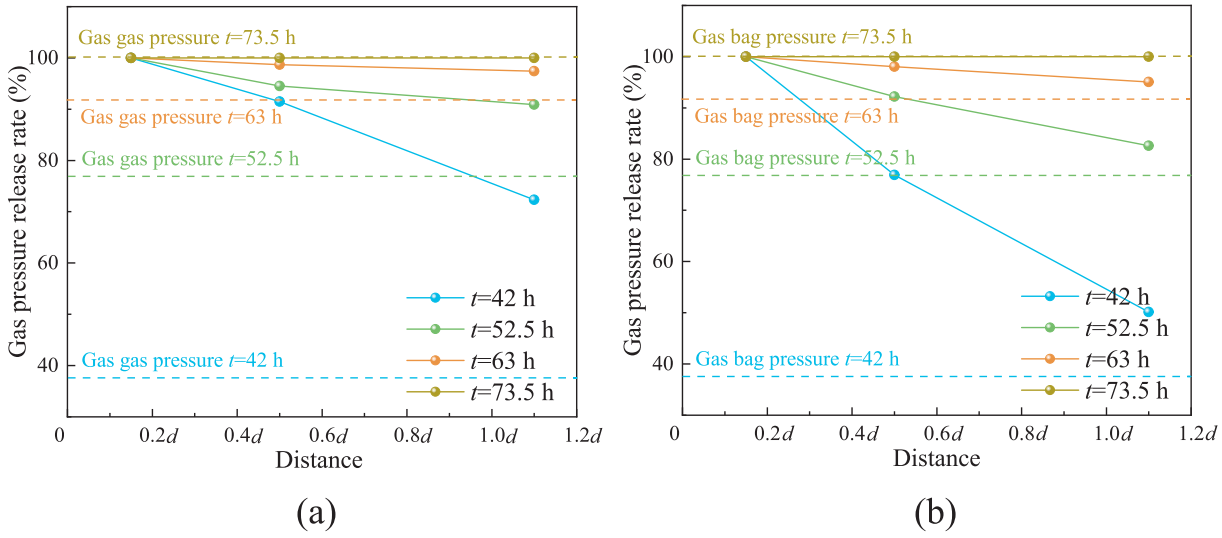

Fig. 12. Radial gas pressure evolution curves of the surrounding rock during the gas release stage. (a) S3, and (b) S4.

flow velocity due to reduced gas pressure during the gas release process. Additionally, the significant reduction in the gas pressure near the surrounding rock leads to a certain degree of closure in the fracture aperture, which also contributes to a decrease in the gas velocity. (3) Residual gas release stage of the reservoir, where the slope rebounds. The fracture deformation stabilizes in this stage. As the gas pressure further decreases, the reduction in flow velocity increases the viscous resistance between the fractures, causing the magnitude of the velocity to decrease with increasing time.

Furthermore, the analysis reveals that, when the accumulated gas flow volume reaches approximately 1.35 m^3, the gas release characteristics enter stage 3. However, at this stage, the outflowing gas accounts for approximately 60% of the total gas volume. This is primarily due to a portion of the gas already flowing into the model from the gas tank before tunnel excavation, which results in a decrease at the monitoring position. Therefore, the flow meter monitors a flow rate that is lower than the actual amount of stored gas.

4 Computational model for the gas migration and release evolution of magmatic rock reservoir

4.1 Fluid–solid coupling calculation model considering damage effects

Based on Hooke's law, by establishing the stress equilibrium, geometric, and deformation compatibility equations in Eq. (7), the fluid–solid coupling control equation (Eq. (8)) can be derived (Li & Liu, 2021).

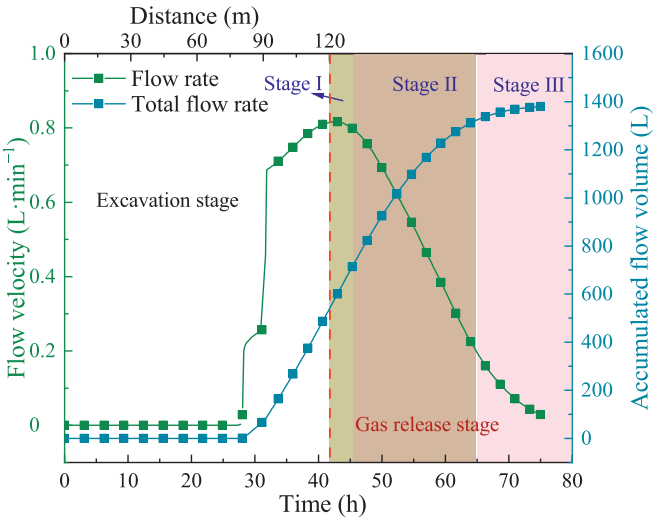

Fig. 13. Evolution curves of the gas flow velocity and accumulated flow volume at the far end of the reservoir during the entire tunnel excavation process.

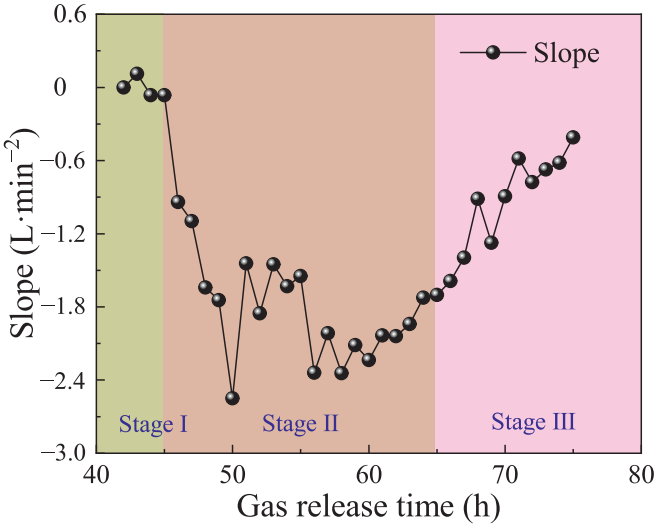

Fig. 14. Variation of the slope of the gas flow rate curve with time.

$$\begin{cases} \boldsymbol{\sigma}_{ij,j} + \boldsymbol{F}_i = 0 \\ \boldsymbol{\varepsilon}_{ij} = \frac{1}{2}\left(\boldsymbol{u}_{i,j} + \boldsymbol{u}_{j,i}\right) \\ \boldsymbol{\sigma}'_{ij} = \lambda \boldsymbol{\delta}_{ij}\boldsymbol{\varepsilon}_v + 2G\boldsymbol{\varepsilon}_{ij} - \alpha p \boldsymbol{\delta}_{ij} \end{cases}, \tag{7}$$

$$Gu_{i,jj} + \frac{G}{1-2\mu} u_{j,ji} + \alpha p_{,i} + F_i = 0, \tag{8}$$

where σ_{ij} is the stress tensor component, σ_{ij}' is the effective stress tensor component, F_i is the body stress in the ith direction, ε_{ij} is the strain tensor component, u_i is the displacement in the ith direction, δ_{ij} is the Kronecker symbol, p is the seepage pressure, and α is the Boit's coefficient. $G = E/[2(1+\mu)]$, $\lambda = E\mu/[(1+\mu)(1-2\mu)]$, and μ is the Poisson's ratio.

Gas seepage in the rock mass occurs through both pores and fractures, and the seepage evolution equations are presented in Eqs. (9) and (10). The relationship between the seepage velocity and gas pressure is given by Eq. (11) (Liu et al., 2024).

$$\rho S_p \frac{\partial \rho}{\partial t} + \nabla \cdot (\rho U) = Q_m, \tag{9}$$

$$e_n \frac{\partial}{\partial t}(\phi_f \rho) + \nabla_T \cdot (e_n \rho U) = e_n Q_m, \tag{10}$$

$$U = -\frac{k}{\mu_g}\nabla p, \tag{11}$$

where ρ is the fluid density, S_p denotes the storage characteristic of the rock medium, calculated as $S_p = \Phi\chi_f$, where Φ is the rock matrix porosity and χ_f is the fluid compressibility. U indicates the flow velocity, e_n represents the fracture aperture, Q_m is the source term, μ_g is the dynamic viscosity, and k is the permeability of the rock mass.

For the seepage process, the porous rock media is modeled using Darcy's law and the fractured media using the cubic law. Research has demonstrated that the fracture aperture correlates with the normal stress, as shown in Eq. (12), and the fracture permeability can be derived, as shown in Eq. (13) (Kong et al., 2018).

$$e_n = e_{n0} \exp\left(-\lambda \frac{(\sigma_3 - p)}{k_n}\right), \tag{12}$$

$$K_f = \frac{e_n^2}{12 f_f}, \tag{13}$$

where e_{n0} represents the initial fracture aperture, k_n is the normal stiffness of the fracture surface, λ is the coefficient reflecting the gas state, where the smaller the value, the higher the gas fluidity, K_f denotes the fracture permeability, and f_f is the roughness coefficient. The effect of roughness on seepage was ignored in this study by setting $f_f = 1$.

In deep strata, the excavation-induced unloading significantly increases the deviatoric stress, which results in damage to the rock mass. The damage evaluation follows the maximum tensile stress and Mohr–Coulomb criteria, with the stress state judgment expressed in Eq. (14) (Lei et al., 2021).

$$\begin{cases} F_1 = -\sigma_3 - f_{t0} \\ F_2 = \sigma_1 - \sigma_3 \frac{1+\sin\varphi}{1-\sin\varphi} - f_{c0} \end{cases}. \tag{14}$$

In this equation, f_{t0} represents the uniaxial tensile strength, f_{c0} represents the uniaxial compressive strength, φ represents the internal friction angle, σ_1 represents the major principal stress, and σ_3 represents the minor principal stress. F_1 corresponds to the tensile stress criterion and results in tensile damage when $F_1 \geq 0$, and F_2 corresponds to the shear stress criterion, where shear damage occurs when $F_2 \geq 0$. Considering the brittle characteristics of the igneous rock mass in the tunnel surroundings, the tensile damage is prioritized when both criteria are satisfied. The damage is regarded as irreversible, and its computation is as follows:

$$D=\begin{cases}0 & F_1<0 \quad F_2<0\\ 1-\left|\frac{\varepsilon_{t0}}{\varepsilon_3}\right|^n & F_1=0 \quad \mathrm{d}F_1>0\\ 1-\left|\frac{\varepsilon_{c0}}{\varepsilon_1}\right|^n & F_2=0 \quad \mathrm{d}F_2>0\end{cases}, \tag{15}$$

where D represents the damage amount, n is the damage coefficient, and ε_{t0} and ε_{c0} are the maximum uniaxial tensile strain and maximum uniaxial compressive strain, respectively.

The effects of damage on three key rock mass parameters (elastic modulus, permeability, and porosity) were primarily investigated in this study. The damage-induced variations in these parameters are characterized as follows:

$$E=(1-D)E_0, \tag{16}$$

$$\phi=\phi_0+D(\phi_r-\phi_0), \tag{17}$$

$$k=k_0\left(\frac{\phi}{\phi_0}\right)^3 \mathrm{e}^{\alpha_k D}, \tag{18}$$

where E_0 is the initial elastic modulus, Φ_0 is the initial porosity, Φ_r is the porosity after failure, k_0 is the initial permeability of the rock mass, and α_k is the damage sensitivity coefficient of permeability, which is taken as $5\times10^{-8}\,\mathrm{Pa}^{-1}$.

4.2 Computational model for reservoir gas pressure distribution based on the ideal gas law

Previous studies have employed two fluid pressure boundary conditions for rock mass flows (Chen et al., 2021; Tu et al., 2024; Wang et al., 2024): (1) constant pressure for infinite reservoirs (water or mud inrush analysis in the surrounding rock) and (2) constant-rate mass source for gas desorption (conventional gas reservoirs). However, magmatic gas reservoirs exhibit distinct characteristics: the finite gas volume leads to dynamic pressure boundaries and the low-porosity rock confines gas storage primarily to fractures, precluding continuous source modeling.

Based on the characteristics of magmatic rock gas reservoirs, a method was proposed in this study to compute the gas pressure distribution using the ideal gas law. The following assumptions were made before applying this method: (1) the gas density after flowing out from the surrounding rock at the tunnel face was equal to the atmospheric gas density, (2) the gas temperature remained constant during seepage, and (3) the gas escaped only at the tunnel face.

This method first calculates the gas volume and corresponding amount of substance in the initial state of the reservoir using Eqs. (19) and (20). Subsequently, by integrating the gas outflow from the tunnel face using Eq. (21), the total amount of gas escaping from the reservoir is obtained (Eq. (22)). Finally, the remaining gas pressure in the reservoir at a given time is calculated using the ideal gas law (Eq. (23)), thereby enabling the real-time dynamic evolution of the gas pressure in the reservoir, as illustrated in Fig. 15.

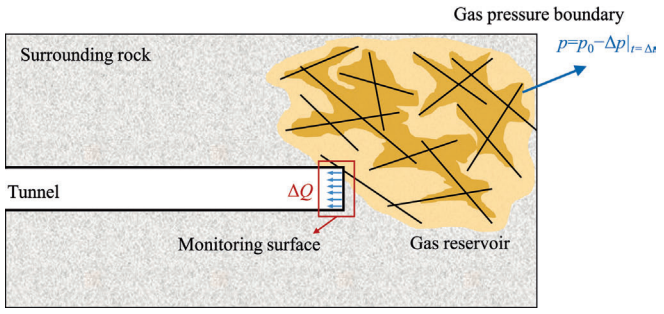

Fig. 15. Schematic diagram of the computational model.

$$Q_g=\frac{Q_0\rho_0}{\rho_g}, \tag{19}$$

$$N_0=\frac{Q_0\rho_0}{M}, \tag{20}$$

$$\Delta Q=\int_\Omega (U_f+U_r)\mathrm{d}t, \tag{21}$$

$$\Delta N=\frac{\Delta Q\rho_0}{M}, \tag{22}$$

$$p=\begin{cases}\frac{(N_0-\Delta N)RT}{V_g} & \Delta N\le N_0\\ 0 & \Delta N>N_0\end{cases}, \tag{23}$$

where Q_g denotes the gas volume in the reservoir, Q_0 refers to the gas volume under atmospheric pressure, ΔQ is the volume of gas outflow from the tunnel face, ρ_g is the gas density in the reservoir, ρ_0 is the gas density under atmospheric pressure, N_0 represents the initial amount of gas in the reservoir, and ΔN is the amount of gas released from the tunnel face. U_f and U_r are the gas flow velocities in the fractures and rock pores at the tunnel face, respectively. M is the molar mass of the gas, Ω is the integral domain, t is the time, R is the ideal gas constant (8.314 J/(mol·K)), and T is the temperature (taken as 298.15 K).

4.3 Fully coupled model for tunnel excavation and seepage considering both time and rock damage effects

The entire tunnel excavation process affects the seepage in the surrounding rock, which is not only related to stress states and gas occurrence conditions, but also closely linked to the seepage time due to the gas release at the tunnel face. Assuming no creep, the surrounding rock damage is considered to be stress-dependent and time-independent, and therefore, steady-state analysis is commonly used to study the deformation and stability under fluid–solid coupling. However, for gas desorption or seepage behavior in rock masses, the seepage evolution depends on both stress and time, making transient analysis more suitable. Nevertheless, traditional studies have failed to effectively integrate the coupled evolution processes of deformation, damage, seepage, and time under deep tunnel excavation conditions.

Hence, a fully coupled tunnel excavation–seepage model was proposed in this study based on steady-state–transient iterative computations. This method was implemented using COMSOL Multiphysics numerical simulation software. This software typically addresses multiphysics problems by decomposing them into multiple subphysics fields for distributed solving, ultimately achieving convergence through iterative approaches. Based on this computational characteristic, the physical field was divided into two parts: damage and stress analysis under fluid–solid interactions and transient evolution of seepage flow accounting for damage effects. An iterative process was employed to resolve the coupled evolution of all physical quantities under their mutual influence. The steady-state simulations primarily determined the stress and damage fields induced by the tunnel excavation, whereas the transient simulations captured the time-dependent evolution of the seepage and stress fields. The iterative exchange of the physical field variables between different computational steps ensured full coupling throughout the process. The main computational steps are outlined as follows: (1) Initial stage: Input the model's physical parameters and apply the initial boundary conditions (e.g., stress, displacement, and constraints). Perform transient calculations to obtain the initial geostress and seepage fields. (2) Steady excavation stage: Import the initial stress and seepage fields as the boundary conditions and define the tunnel excavation increment. Perform steady-state calculations to determine the excavation-induced stress and damage fields. (3) Transient excavation stage: Import the stress and damage fields from the steady-state step as the boundary conditions. In addition, use the seepage field from the previous transient step as the initial boundary condition. Define the time increment and initial gas outflow, and conduct transient calculations to obtain the updated stress and seepage fields. (4) Repeat steps (2) and (3) until the tunnel excavation is completed. The detailed computational process is illustrated in Fig. 16.

5 Characteristics of gas release during tunnel excavation and optimization measures for the exhaust borehole in the tunnel face

5.1 Selection of computational parameters and verification of the results

The numerical simulations were performed using COMSOL Multiphysics. Prior to the simulations, the following assumptions were made: (1) the rock strength followed a Weibull distribution, (2) the fractures were smooth and flat, neglecting the roughness effects on seepage, and (3) the tunnel was sealed with initial support and gas could only escape from the tunnel face.

Figure 17 illustrates the model dimensions, which are 60 m × 60 m × 120 m. The stratification dip angle of the rock layers is 45°, and the fractures within the reservoir are randomly distributed on the right side of the model. The tunnel (height × width: 6.5 m × 6.8 m) is excavated at a rate of 10 m per step (2 days/step) with a gas exhaust borehole 90 m along the excavation direction. The model boundaries are as follows: fixed bottom, roller side supports, top geostress load, and tunnel burial depth of approximately 900 m (corresponding to an overburden stress of approximately 25 MPa). The reservoir fracture boundary has an initial gas pressure of 3 MPa. A tetrahedral mesh is used for the model, the fractures are represented by thin elastic layers, and the gas outflow is monitored only at the tunnel face.

To investigate the gas migration characteristics in the surrounding rock during the entire tunnel excavation process in magmatic formations and to optimize the gas exhaust measures, five working conditions were designed with different exhaust borehole areas, as shown in Table 2 (where condition 1 corresponds to the physical model test). Notably, in actual field construction, 20 exhaust boreholes (diameter: 0.1 m, depth: 10 m) yield a total borehole area of approximately 0.16 m^2. However, due to the small field borehole diameter relative to the numerical model dimensions, it is difficult to simulate the gas exhaust using an exact field configuration.

Drilling drainage primarily aims to enhance gas release efficiency by increasing the exposed area. Thus, maintaining drill hole area consistency between the numerical simulations and prototype is of utmost priority. For this reason, an equivalent area method was adopted in this study, where three exhaust boreholes were set in the numerical model (one on the upper part and the remaining two in the middle part of the tunnel face), with equivalent exhaust areas of 0, 0.08, 0.16, 0.24, and 0.32 m^2. Furthermore, in practical construction, the locations of the boreholes also exert a certain effect on the effectiveness of gas drainage. However, since this study was primarily focused on investigating the effect of the exhaust borehole area on the gas release, all exhaust boreholes were maintained at identical positions across different borehole areas, thereby excluding the effects caused by variations in exhaust borehole locations.

The fundamental physical and mechanical parameters of the rock mass used in the numerical simulations were obtained from laboratory tests. The uniaxial compressive and tensile strengths were 144 and 5.6 MPa, respectively, with an elastic modulus of 25.5 GPa and an internal friction angle of 55°. To determine the seepage parameters of the fractured rock mass, gas flow tests were conducted at a gas pressure of 3 MPa, and the results are shown in Fig. 18. The gas state parameter λ and the stiffness coefficient k_n were obtained by fitting the equations in Fig. 18 (b), where the initial fracture aperture e_0 was set as 2×10^{-6} m.

Previous studies have shown that the aperture of jointed rock mass fractures in strata typically ranges from 10^{-5} to 10^{-7} m, while those in reservoir fractures usually exceed 10^{-4} m. Accordingly, the initial aperture of fractures in the strata was set to 2×10^{-6} m, and that of reservoir

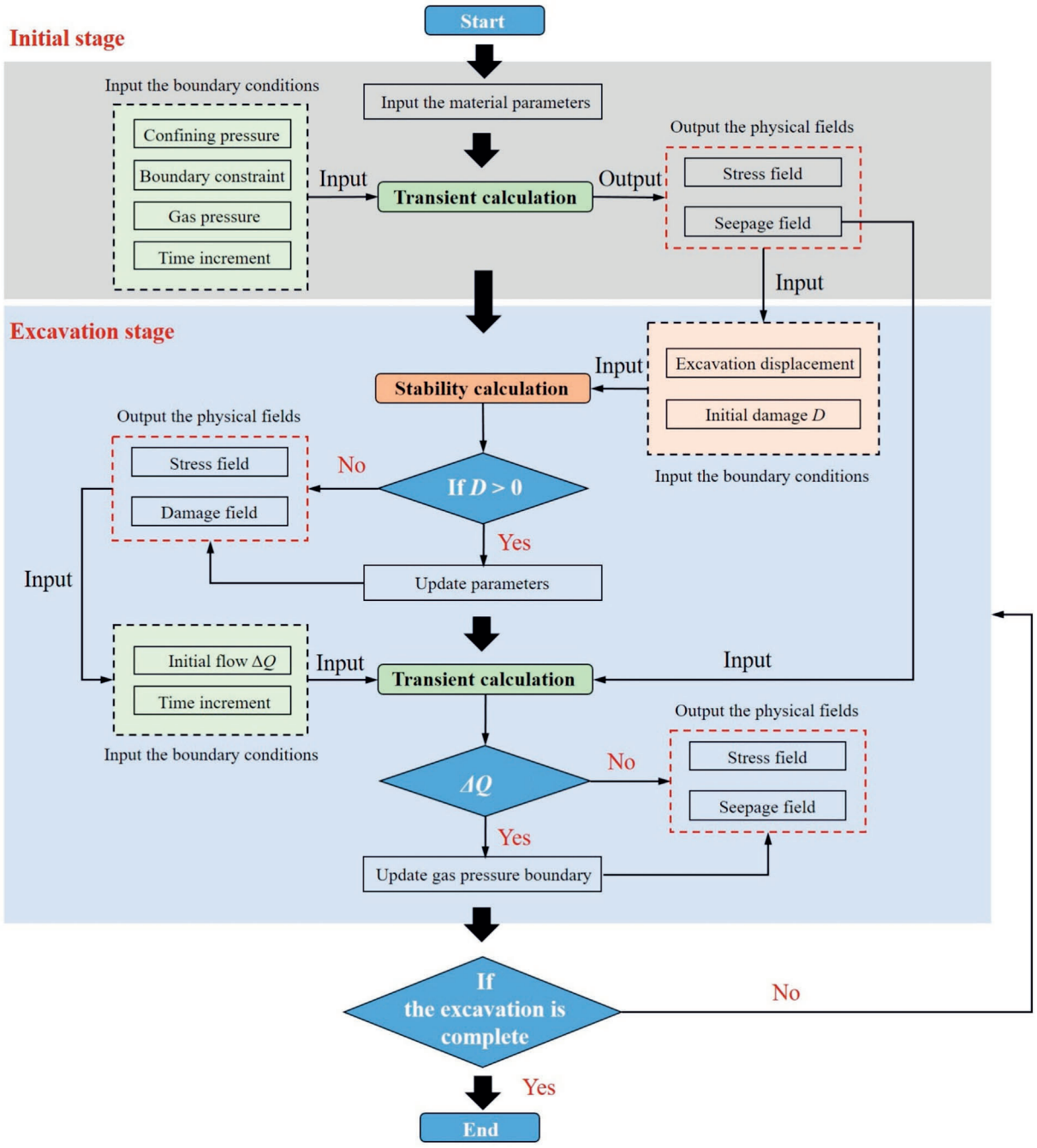

Fig. 16. Flow chart of the computational process.

fractures was set to 2×10^{-4} m in the numerical model. As for the porous matrix, existing studies suggest that the porosity of granite generally ranges from 0.1% to 2%, and the permeability of intact granite is approximately 10^{-18} to 10^{-19} m^2 (Cassiaux et al., 2006; Surma & Geraud, 2003). Therefore, a porosity of 0.5% and an initial permeability of 10^{-19} m^2 were adopted in this study. Details of the parameters used in the numerical simulations are provided in Table 3.

To validate the accuracy of the numerical simulation results, the results of condition (1) were compared with those from the physical model tests. Given the differences in scale between the physical model tests and numerical simulations, normalization was applied for comparison. The normalized results are shown in Fig. 19. As the flow measurement point in the physical model test was located inside the gas tank, it could not capture the total time required for complete gas release. Therefore, the time corresponding to the transition into stage 3 of gas release was used as a reference for normalization. The physical model test entered stage 3 at 24.5 h, whereas the numerical model predicted this transition at 70 days.

The gas flow volume curves for both cases showed a transition from a rapid to a slow increase with time, and

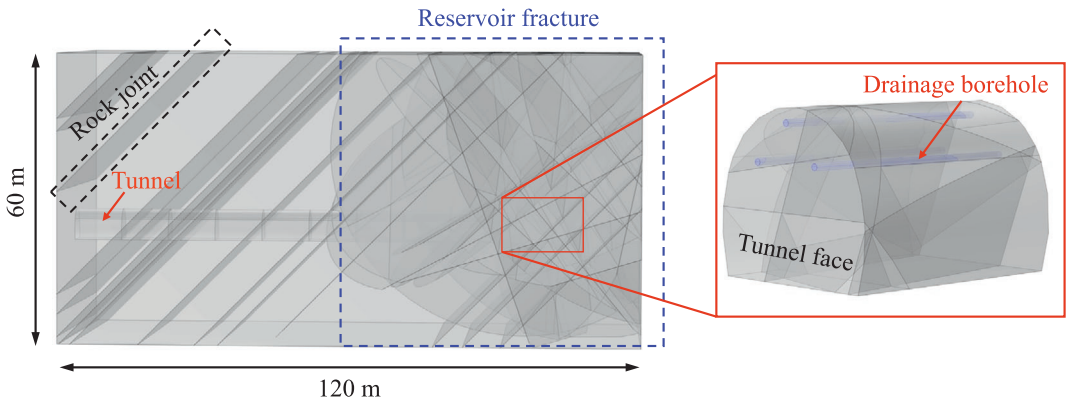

Fig. 17. Size information of the model.

Table 2
Working conditions used in the numerical simulations.

No.	Geostress (MPa)	Gas pressure (MPa)	Length of borehole (m)	Diameter of borehole (m)	Borehole area (m^2)
1	25	3	0	0	0
2	25	3	10	0.18	0.08
3	25	3	10	0.26	0.16
4	25	3	10	0.32	0.24
5	25	3	10	0.36	0.32

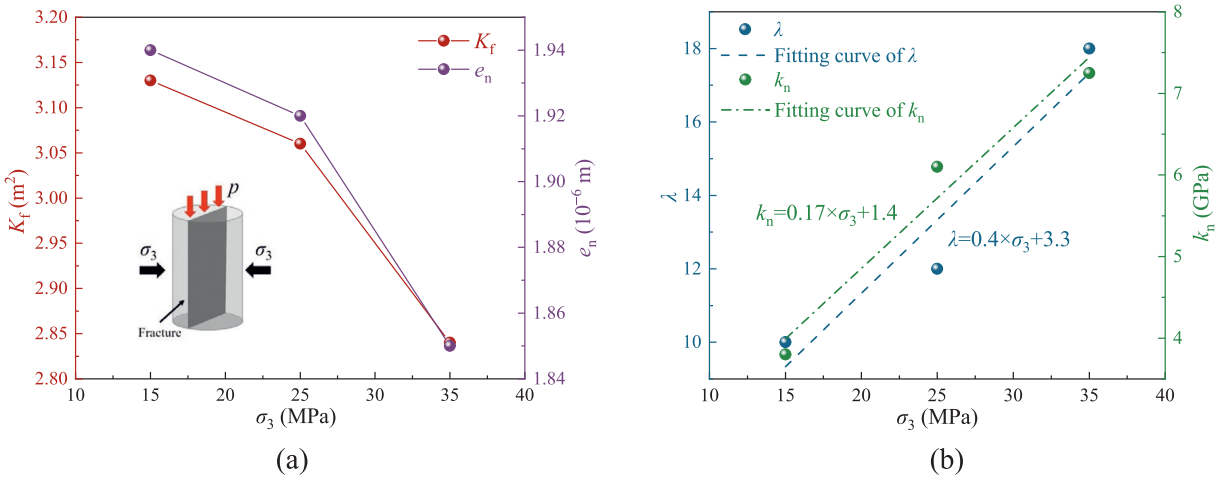

Fig. 18. Variations in the permeability of the fractured rock mass under a gas pressure of 3 MPa. (a) Variations of the permeability with the confining pressure, and (b) variations of parameters k_n and λ.

Table 3
Parameters used in the numerical simulations.

Parameter	Value	Parameter	Value
Uniaxial compressive strength, f_{c0}	144 MPa	Rock initial porosity, Φ_{r0}	0.005
Uniaxial tensile strength, f_{t0}	5.6 MPa	Rock residual porosity, Φ_{rr}	0.8
Elastic modulus, E	25.5 GPa	Rock initial permeability, K_{r0}	1×10^{-19} m^2
Internal friction angle, φ	55°	CO_2 dynamic viscosity, μ_c	1.46×10^{-5} Pa·s
Damage coefficient, n	2	Fracture porosity, φ_{f0}	1
Initial amount of gas, Q_0	5×10^6 m^3	Rock joint initial aperture, e_{j0}	2×10^{-6} m
		Reservoir fracture initial aperture, e_{f0}	2×10^{-4} m

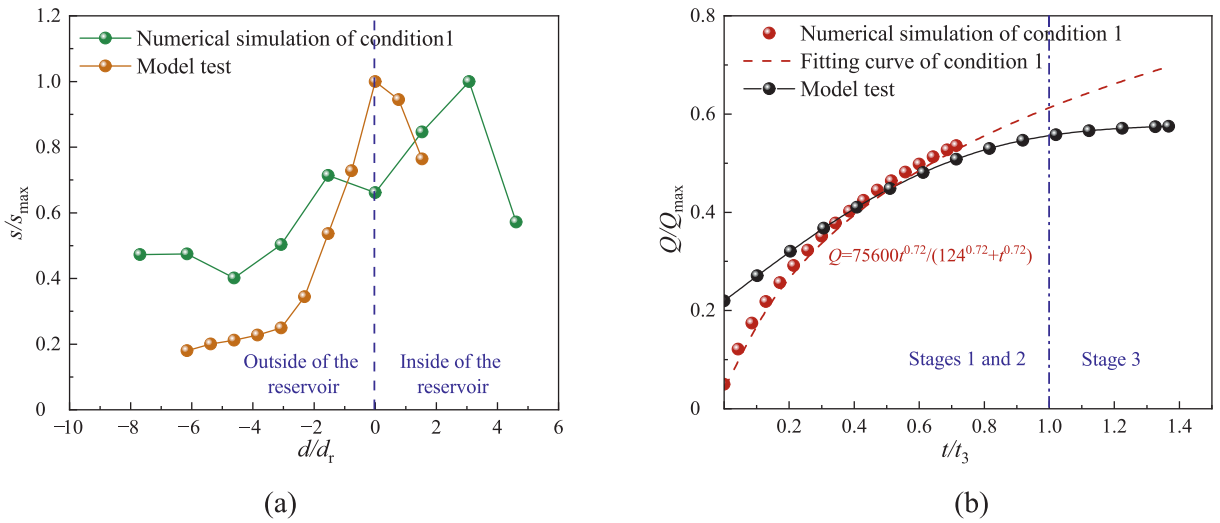

Fig. 19. Comparison between the numerical simulations and physical model tests. (a) Comparison of displacement, and (b) comparison of gas flow volume during the release stage. (s_{max} represents the maximum deformation value, Q_{max} represents the gas storage volume, d_r represents the reservoir location, and t_3 represents the time when the gas release reaches stage 3).

stage 3 began when about 50%–60% of the gas had been released. However, the flow rate in the numerical simulations after entering stage 3 was higher than that in the physical model tests, which is likely because the physical model test fails to detect the gas already stored in the rock layers. Analysis of the normalized displacement curves shows consistent trends in both methods, where the settlement increases as the tunnel face approaches the reservoir, with a sharp increase observed upon entering the fractured reservoir. The numerical differences are caused by the testing methods used in the experiments and the size effects between the prototype and model. These differences do not affect the experimental trends, but only result in numerical discrepancies. In summary, the numerical simulations closely match the physical model tests in terms of the deformation trends and gas release characteristics, confirming its reliability in describing gas migration and release during tunnel excavation.

5.2 Evolution of gas migration and release during the tunnel excavation process

Figure 20 shows the evolution of the tunnel deformation and damage during excavation. Both the face damage and vault deformation increase as the tunnel approaches the reservoir. Once the tunnel enters the reservoir, both the face damage and vault deformation reach their maximum values. Damage distribution is fracture-dependent: when intersecting the reservoir, the damage concentrates near fractures, particularly in the upper-central face due to stronger excavation-induced unloading effects.

Tunnel excavation-induced unloading not only causes damage to the surrounding rock, thereby increasing its permeability, but also affects the aperture of fractures. To analyze the influence of excavation unloading on the fracture aperture at the tunnel face, the evolution curves of the fracture aperture and bar charts of the normal stress are shown in Fig. 21. Analysis of the normal stress evolution indicates that, before tunnel excavation, the fracture normal stress outside the reservoir is generally higher than that inside. After tunnel excavation, the normal stress on the fractures outside the reservoir decreases by approximately 30%, whereas that within the reservoir only decreases by about 9%–17%, indicating that a higher geostress leads to stronger unloading effects.

Further analysis shows that the fracture aperture variation correlates positively with changes in the normal stress. Before reservoir entry, excavation unloading increases the fracture aperture by 17%–25%, whereas the post entry fracture aperture increments are smaller (4%–7%). Despite the lower relative growth, the reservoir fractures exhibited a larger absolute increase due to their initially higher apertures (e.g., 2.6×10^{-7} m at 10 m vs. 9.1×10^{-6} m at 80 m). Thus, the excavation unloading affects the aperture, whereas the initial aperture dominates the seepage behavior.

To investigate the gas release behavior at the tunnel face during the entire excavation process, the evolution curves of the gas flow volume over time are plotted in Fig. 22. During tunnel excavation, the gas flow volume at the tunnel face exhibits a stepwise increasing trend as the tunnel face approaches the reservoir. Within each excavation increment, the gas flow volume initially increases rapidly and then more gradually. Furthermore, analysis of the gas flow volume curves reveals that the cumulative gas release from the tunnel face before intersecting the reservoir fractures is only about 0.006 m^3, indicating excellent sealing capacity of the magmatic rock gas reservoir. Significant gas release occurs only when the tunnel face intersects reservoir fractures or when excavation-induced damage connects directly with the reservoir.

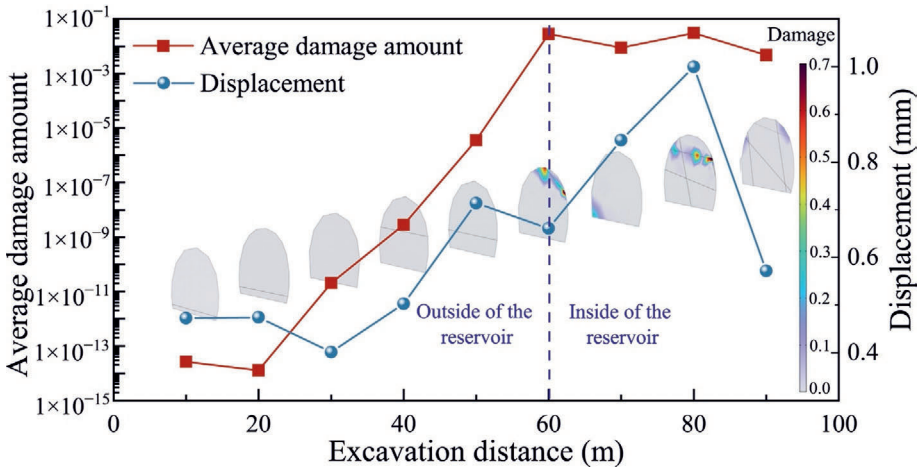

Fig. 20. Evolution curves of the deformation and damage of the tunnel during excavation.

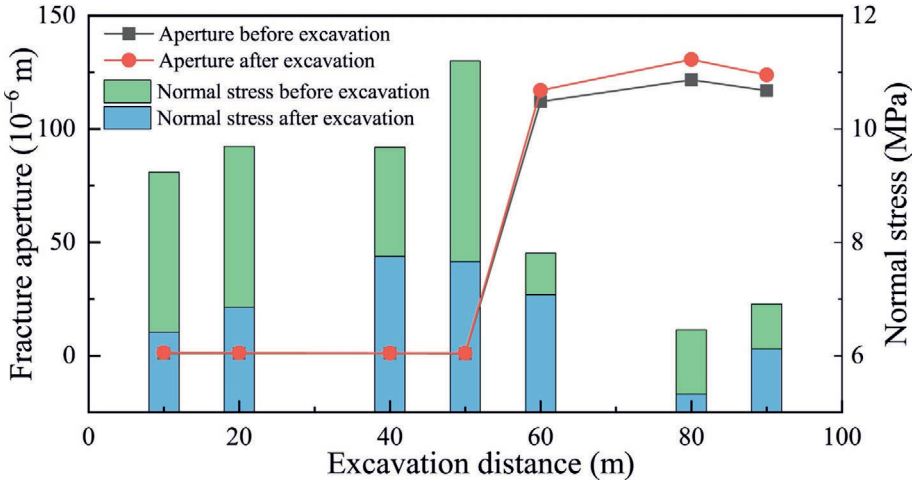

Fig. 21. Evolution curves of the fracture aperture and bar charts of the normal stress.

Gas release analysis reveals distinct sources before and after the tunnel face intersects with the reservoir. Pre-intersection, the gas releases at the tunnel face primarily originate from the rock matrix pores (where the fractures contribute only about 4% of the total) as most extra reservoir fractures lack connectivity and rapidly deplete upon excavation. Post-intersection, the reservoir fractures dominate (60%–94% of the total), where the emission rates were positively correlated with the fracture density, but were negatively affected by excavation-induced damage.

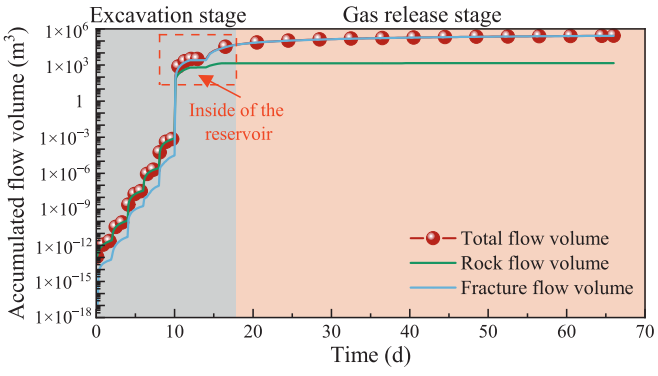

Fig. 22. Evolution curves of the gas flow volume over time.

During the gas release stage, the gas flow volume initially increases rapidly and then gradually. The proportion of gas escaping through the fractures increases from 94% to 99% as the release time progresses, indicating that in dual-permeability media comprising fractures and pores, changes in the gas pressure have a greater effect on the pore flow than on the fracture flow.

The gas seepage evolution at the tunnel face was examined at three characteristic excavation positions: 20 m (pre-reservoir), 60 m (reservoir contact), and 90 m (reservoir entry). Figure 23 shows the corresponding gas flow velocity and pressure variations. Distinct release patterns emerged: at 20 m, both the pore and fracture flow velocities decreased post excavation, where the rock matrix exhibited a slower rate of decline than the fractures. The initial gas pressure was 0.2 Pa before dropping abruptly to zero upon excavation.

At the reservoir intersection during tunnel excavation, distinct gas flow velocity patterns emerge between the rock matrix and fractures. In the rock matrix, the gas flow velocity initially drops rapidly before stabilizing, whereas the gas flow velocity in the fractures first surges and then declines gradually. This is because the gas stored in the rock is under relatively high pressure. After tunnel excavation, due to rock damage and pressure differences between the tunnel face and surrounding rock, the limited gas within the rock is rapidly released, leading to a rapid drop in the gas flow velocity. Conversely, fractures contain greater gas volumes that cannot escape immediately. Driven by these pressure differences, the gas flow velocity in the fractures rises quickly, and then gradually decreases as the gas content diminishes. At this location, most of the gas near the tunnel face is concentrated in the fractures. With

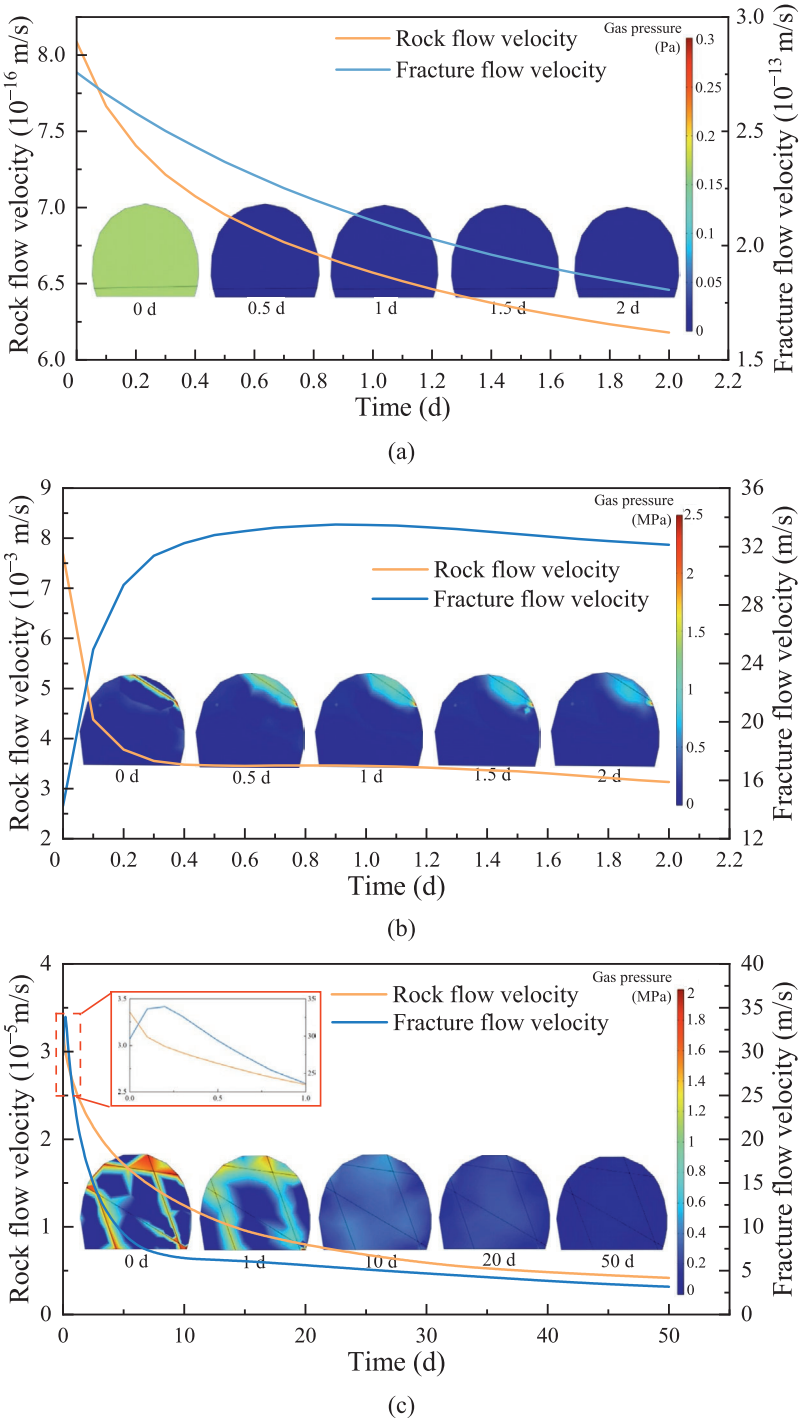

Fig. 23. Evolution curves of the gas flow velocity and gas pressure. (a) 20 m, (b) 60 m, and (c) 90 m.

continued release, the pressure of the stored gas drops from 2.5 MPa to 0.8 MPa within 2 days after tunnel excavation.

Once the tunnel face enters the reservoir, the evolution of the gas flow velocity at the tunnel face is consistent with that observed when the tunnel reaches the reservoir. However, because of the higher fracture density at the tunnel face, the attenuation of the fracture flow velocity is faster than before. Additionally, during long-term release, it is observed that rapid gas release from the face fractures mainly occurs within 10 days after tunnel excavation, primarily resulting from the release of gas stored in the surrounding fractures. Subsequently, with the supplement of the gas sources, the flow velocity enters a relatively stable declining phase.

5.3 Effect of exhaust boreholes on the gas release of reservoirs

The effect of the exhaust borehole area on the gas release efficiency was examined at an excavation distance of 90 m (Fig. 24). It can be observed that gas flow volume declined over time across all borehole configurations. Without boreholes (0 m^2), the gas escaped predominantly through the fractures. As the exhaust borehole area increases, the proportion of gas escaping from the fractures relative to the total amount released decreases accordingly. When the exhaust borehole area is 0.32 m^2, the proportion of fracture-released gas accounts for approximately 72% of the total after 50 days of release.

Figure 25 illustrates the nonlinear relationship between the exhaust borehole area and gas flow volume after 50 days. The gas flow volume exhibits an "S-shaped" trend with increasing exhaust borehole area. This is primarily because, for smaller borehole areas, the gas release increases nonlinearly as the fracture outflow exceeds the borehole discharge capacity. As the borehole area continues to increase and surpasses the internal fracture outflow, the gas release volume becomes controlled by the internal fractures. Consequently, the efficiency of gas extraction decreases with a further increase in the exhaust borehole area. When the exhaust borehole area reaches a value of 0.24 m^2, the maximum gas release efficiency is achieved, with an enhancement of approximately 21.7%. However, when the exhaust borehole area increases to 0.32 m^2, the gas release rate only improves by 24.6%, showing a noticeable decline in the gas release efficiency with a further increase in the exhaust borehole area.

Additionally, an analysis of the gas release curves for different exhaust borehole areas shows that the gas flow volume through the exhaust boreholes increases with the borehole area, whereas the gas flow volume in the fractures decreases. This is primarily because the presence of exhaust boreholes enhances the gas escape efficiency near the tunnel face, thereby reducing the gas storage pressure and slowing

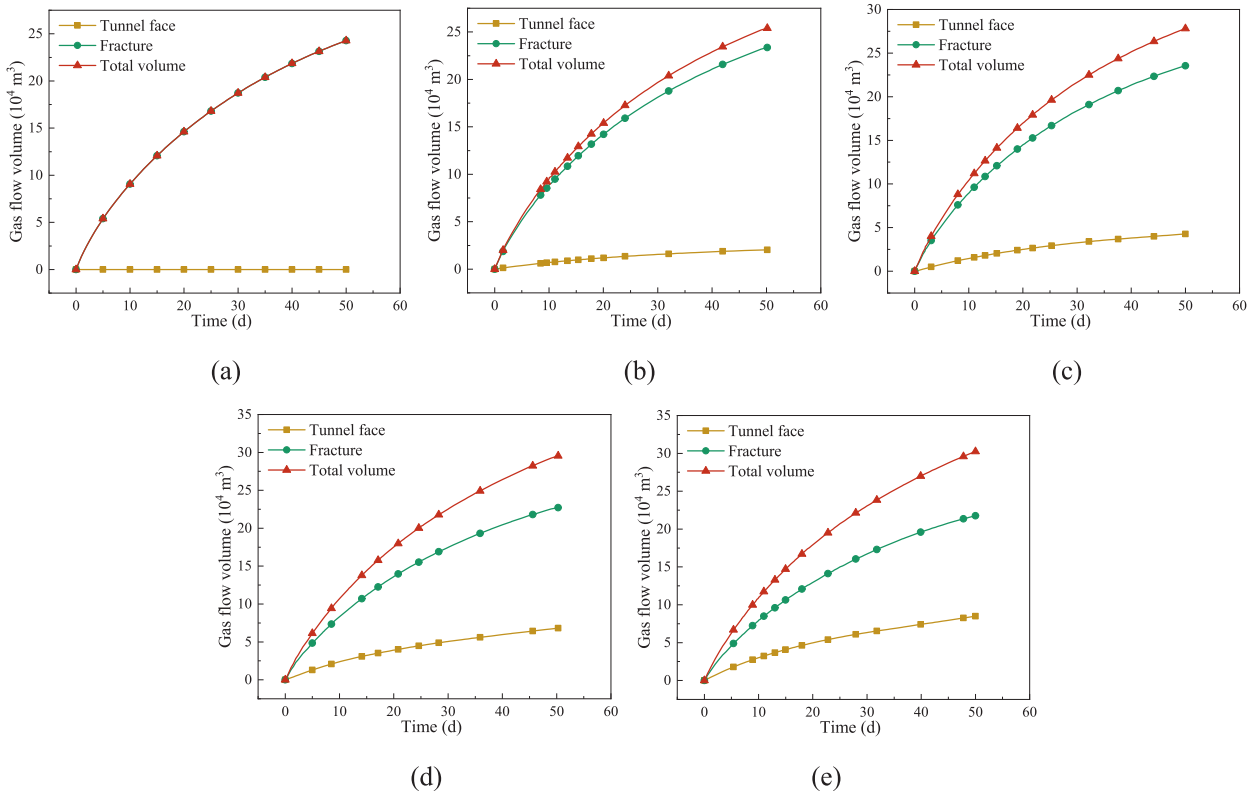

Fig. 24. Evolution curves of the gas flow volume over time. (a) Borehole area: 0 m^2, (b) borehole area: 0.08 m^2, (c) borehole area: 0.16 m^2, (d) borehole area: 0.24 m^2, and (e) borehole area: 0.32 m^2.

down the gas migration within the fractures. When the exhaust borehole area reaches a value of 0.32 m^2, the fracture gas flow volume decreases by approximately 10% compared with that without exhaust boreholes.

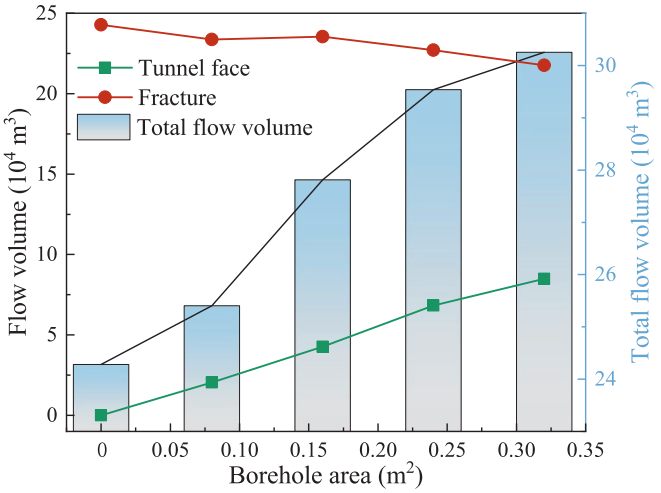

Fig. 25. Evolution curves of the gas flow volume with the exhaust borehole area.

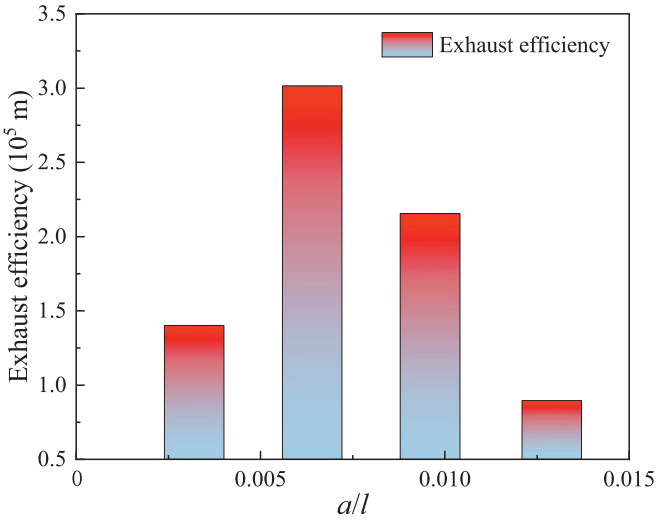

Fig. 26. Relationship between the gas release efficiency and ratio of the exhaust borehole area to the total fracture trace length *a*/*l*.

Further analysis of the relationship between the exhaust borehole area and gas release efficiency (the slope of the total flow volume curve in Fig. 25) shows that the gas release from exhaust boreholes is positively correlated with the degree of fracture development in the surrounding rock. Therefore, the ratio of the exhaust borehole area (a) to the total fracture trace length (l) is used as an evaluation metric to evaluate the exhaust efficiency. The results shown in Fig. 26 indicate that the gas release efficiency initially increases and then decreases with increasing exhaust borehole area. The highest gas release efficiency occurs when the l/a ratio is between 0.064 and 0.096.

To analyze the evolution of reservoir gas pressure influenced by gas release at the tunnel face, the case with an exhaust borehole area of 0.32 m^2 is selected. The evolution of the gas pressure drop in the surrounding rock at different release times is shown in Fig. 27. It can be seen that the pressure drop is negligible during the early stages of gas release. As the release time increases (e.g., 10 days), a noticeable pressure reduction occurs within approximately twice the tunnel diameter, primarily concentrated in the fractures directly intersecting the tunnel. With further extension of the release time (e.g., 50 days), the gas content in the reservoir significantly decreases, leading to a general drop in gas pressure throughout the reservoir, while the most pronounced pressure drop still occurs in the fractures intersecting the tunnel.

Figure 28 presents the evolution of the gas pressure drop in the rock strata after 50 days of gas release for different exhaust borehole areas. The pressure drop in the strata increases with the enlargement of the exhaust borehole area. When no exhaust hole is installed at the tunnel face, the maximum gas pressure drop after 50 days of release is approximately 2.2 MPa, indicating a significant residual gas pressure in the surrounding rock. With the installation of exhaust boreholes, the gas pressure drop around the tunnel is significantly enhanced. For example, when the exhaust borehole area is only 0.08 m^2, the pressure drop reaches about 2.8 MPa. When the exhaust borehole area increases to 0.32 m^2, the gas pressure substantially decreases in most surrounding rock regions, with a maximum drop of 3 MPa. These findings suggest that, for magmatic rock gas reservoirs, setting exhaust boreholes not only shortens the gas release duration, but also significantly

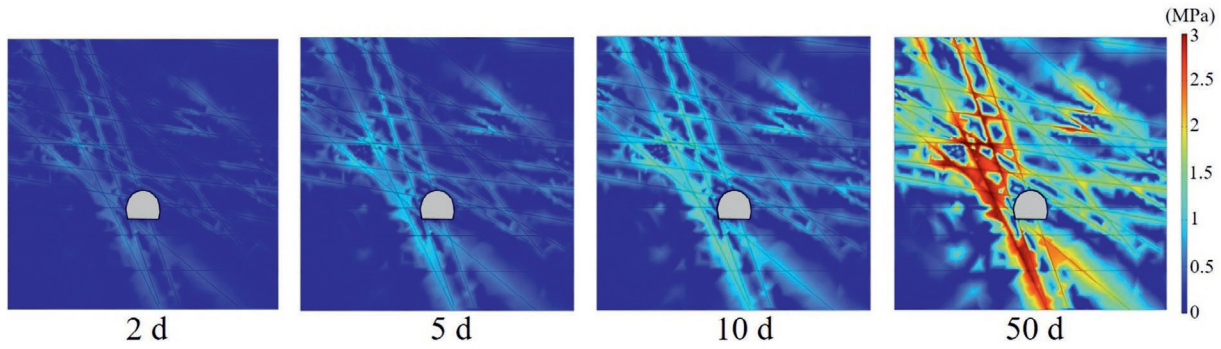

Fig. 27. Evolution of the gas pressure drop in the surrounding rock under different release times.

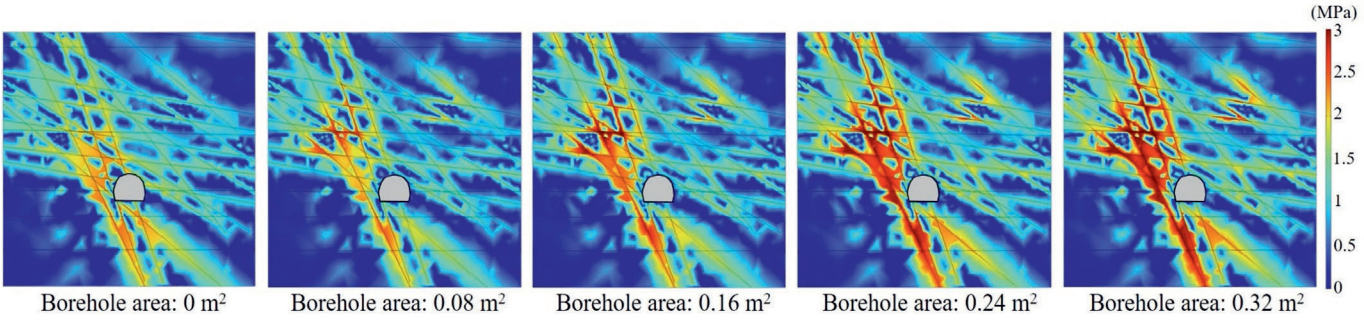

Fig. 28. Evolution of the gas pressure drop in the rock strata after 50 days of gas release for different exhaust borehole areas.

reduces the gas pressure in the surrounding rock near the tunnel face. The evident drainage effect of the exhaust boreholes near the tunnel face provides favorable conditions for subsequent rock grouting and reinforcement operations.

6 Conclusions

(1) The formation of gas reservoirs in magmatic rock formations undergoes the following processes: magmatic intrusion → magmatic condensation with volume contraction to generate fractures and release gases → gas accumulation in the fracture-developed zones → formation of magmatic gas pockets → reduction of fracture space due to tectonic compression of the formation → increase in gas occurrence pressure to form high-pressure reservoirs. These reservoirs are mainly distributed in the Cenozoic magmatic rocks of the Qinghai–Tibet Plateau.

(2) A model testing system was developed to study the gas migration in the surrounding rock. The results showed that deformation increased sharply when the tunnel face–reservoir distance was less than 3*D*, with maximum crown deformation at the intact rock–reservoir interface. As the tunnel was excavated into the reservoir, gas escape led to a further stress release in the surrounding rock (approximately 15% of the total), affecting the vertical stress more than the tangential stress. The gas flow exhibited three stages: stable release stage, gas replenishment stage, and residual gas release stage.

(3) A gas migration–release evolution model was established for a magmatic rock gas reservoir. The pressure distribution in the fractured reservoir was calculated using the ideal gas law, whereas steady-state–transient iterative computations were used to simulate the deformation–seepage evolution during the entire tunnel excavation process, considering the effects of time and rock damage. The numerical results obtained by this method showed good agreement with the outcomes of the model tests.

(4) Before the tunnel entered the reservoir, the gas flow velocity in both the rock matrix and fractures decreased over time after excavation, with gas primarily released from the rock pores. Once the tunnel face contacted the reservoir fractures, the gas flow velocity in the rock matrix initially decreased rapidly and then more gradually, whereas the gas flow velocity in the fractures first increased rapidly and then decreased. The gas escaping from the tunnel face mainly originated from the reservoir fractures, accounting for 60%–94% of the total. In a dual-porosity medium, the pore gas flow was more sensitive to changes in pressure than the fracture flow.

(5) Installing gas exhaust boreholes effectively shortened the gas release duration and significantly reduced the in-situ gas pressure in the surrounding rock near the tunnel. The tunnel face gas flow increased in an "S-shaped" trend with the exhaust borehole area. The optimal gas release efficiency occurred when the ratio of the fracture trace length to the borehole area l/a ranged between 0.064 and 0.096. Additionally, the exhaust boreholes suppressed gas escape from the fractures to a certain extent.

Data availability

The data that support the findings of this study are available from the corresponding author upon reasonable request.

CRediT authorship contribution statement

Jilu Zhang: Writing – original draft, Software, Investigation, Formal analysis, Data curation. **Xiaohan Zhou:** Project administration, Funding acquisition, Data curation. **Xinrong Liu:** Writing – review & editing, Project administration, Methodology, Funding acquisition. **Lei Fang:** Software, Investigation. **Lojain Suliman:** Writing – review & editing. **Guoliang Li:** Project administration.

Declaration of competing interest

The authors declare that they have no known competing financial interests or personal relationships that could have appeared to influence the work reported in this paper.

Acknowledgement

This work is supported by the Chongqing Talents and Outstanding Scientists Project (Grant No. cstc2024ycjh-bgzxm0032), the National Natural Science Foundation of China (Grant No. 52374079), and the Natural Science Foundation of Chongqing (Grant No. CSTB2024NSCQ-MSX0195).

References

Ahmadi, M. H., & Hekmat, M. H. (2021). Numerical and experimental investigation of air flow behavior and H_2S gas release through an inclined traversed tunnel. *Journal of the Brazilian Society of Mechanical Sciences and Engineering, 43*(10).

Cassiaux, M., Proust, D., Siitari-Kauppi, M., Sardini, P., & Leutsch, Y. (2006). Clay minerals formed during propylitic alteration of a granite and their influence on primary porosity: A multi-scale approach. *Clay and Clay Minerals, 54*(5), 541–554.

Chen, C. H., Luo, J., Cao, J., Liang, J., Li, X. C., Cao, T. K., Xu, Y. H., Cai, L. F., Yu, P., & Zhu, T. Y. (2025). A novel method for calculating the dynamic reserves of tight gas wells considering stress sensitivity is under consideration. *Earth Energy Science, 1*(1), 1–8.

Chen, Y. F., Zeng, J., Shi, H. T., Wang, Y. F., Hu, R., Yang, Z. B., & Zhou, C. B. (2021). Variation in hydraulic conductivity of fractured rocks at a dam foundation during operation. *Journal of Rock Mechanics and Geotechnical Engineering, 13*(2), 351–367.

Chen, Z. Y., Su, P. D., Huang, L., Chen, H. D., & Du, Y. B. (2020). Study on monitoring and prevention technique for harmful gas in no.1 inclined shaft of Hongdoushan Tunnel. *Modern Tunneling Technology, 57*(4), 178–184 (in Chinese).

Cheng, L., Ge, Z. L., Chen, J. F., Ding, H., Zou, L. S., & Li, K. (2018). A sequential approach for integrated coal and gas mining of closely-spaced outburst coal seams: Results from a case study including mine safety improvements and greenhouse gas reductions. *Energies, 11*(11).

Cui, J. P., Tao, H., Ren, Z. L., Jin, W., Liu, H., Meng, Z. Y., & Cheng, K. Z. (2022). Genesis and accumulation period of CO_2 gas reservoir in Hailar Basin. *Energies, 15*(17).

Czarny, R., Malinowski, M., Chamarczuk, M., Cwiekala, M., Olechowski, S., Isakow, Z., & Sierodzki, P. (2021). Dispersive seismic waves in a coal seam around the roadway in the presence of excavation damaged zone. *International Journal of Rock Mechanics and Mining Sciences, 148*.

Fang, L., Zhou, X. H., Liu, X. R., Zhang, J. L., Wang, Y., & Suliman, L. (2025). Mechanical behaviors and permeability characteristics of granite considering through-crack inclination and seepage gas pressure. *Theoretical and Applied Fracture Mechanics* (pp. 136).

Fang, Y., Yao, Z. G., & Lei, S. (2019). Air flow and gas dispersion in the forced ventilation of a road tunnel during construction. *Underground Space, 4*(2), 168–179.

Feng, Y., Seol, H., Lee, J. K., & Eun, J. (2023). Numerical analysis of gas-bearing ground deformation and failure mode around the parallel tunnel cross-passage. *In Geo-Congress on Sustainable Infrastructure Solutions from the Ground Up* (541-550). Los Angeles, CA.

Gao, H., Qing, L. B., Ma, G. W., & Zhang, D. C. (2023). Numerical investigation on grout spread and grouting parameter analysis in fracture with flowing water. *Journal of Petroleum Science and Engineering*, 221.

Goff, F., & Janik, C. J. (2002). Gas geochemistry of the Valles caldera region, New Mexico and comparisons with gases at Yellowstone, Long Valley and other geothermal systems. *Journal of Volcanology and Geothermal Research, 116*(3–4), 299–323.

Guo, B. H., Li, Y. Z., Jiao, F., Luo, T., & Ma, Q. (2018). Experimental study on coal and gas outburst and the variation characteristics of gas pressure. *Geomechanics, Geophysics, Geosystems, 4*(4), 355–368.

He, J., Wei, X. Y., & Yin, M. (2023). Study on the long-term performance of shield tunnel passing through the gas-bearing strata. *Underground Space, 9*, 1–19.

Huo, Z. G., Xue, W. T., & Shu, L. Y. (2021). Exploration on outburst mechanism of rock and carbon dioxide in coal mines of China. *Coal Science and Technology, 49*(1), 155–161 (in Chinese).

Ishibashi, T., Asanuma, H., Mukuhira, Y., & Watanabe, N. (2023). Laboratory hydraulic shearing of granitic fractures with surface roughness under stress states of EGS: Permeability changes and energy balance. *International Journal of Rock Mechanics and Mining Sciences, 170*.

Kang, X. B., Xu, M., Luo, S., & Xia, Q. (2013). Study on formation mechanism of gas tunnel in non-coal strata. *Natural Hazards, 66*(2), 291–301.

Kong, Y., Zhu, Z. D., & Ruan, H. N. (2018). Stress-seepage coupling characteristics of jointed rock mass under three principal stresses. *Rock and Soil Mechanics, 39*(6), 2008–2016 (in Chinese).

Lei, Q. H., Doonechaly, N. G., & Tsang, C. F. (2021). Modelling fluid injection-induced fracture activation, damage growth, seismicity occurrence and connectivity change in naturally fractured rocks. *International Journal of Rock Mechanics and Mining Sciences, 138*.

Li, M., & Liu, X. S. (2021). Experimental and numerical investigation of the failure mechanism and permeability evolution of sandstone based on hydro-mechanical coupling. *Journal of Natural Gas Science and Engineering, 95*.

Liu, L., Gao, Y. Q., Qu, X. Y., Meng, Q. A., Gao, F. H., Ren, Y. G., & Zhu, D. F. (2006). Petrology and carbon-oxygen isotope of inorganic CO2 gas reservoir in Wuerxun Depression, Hailaer Basin. *Acta Petrologica Sinica, 22*(8), 2229–2236.

Liu, X. R., Zhang, J. L., Zhou, X. H., Liu, Y. Y., Wang, Y., & Luo, X. Y. (2024). Damage-seepage evolution mechanism of fractured rock masses considering the influence of lateral stress on fracture deformation under loading and unloading process. *Rock Mechanics and Rock Engineering, 57*(12), 10973–10999.

Lu, Y. Y., Zhao, G. L., Ge, Z. L., Jia, Y. Z., Tang, J. R., Gong, T. Y., Huang, S., Li, Z. T., Fu, W. Y., & Mi, J. Y. (2025). Challenges and development direction of deep fragmented soft coalbed methane in China. *Earth Energy Science, 1*(1), 38–64.

Luo, Y., Gong, H. L., Qu, D. X., Li, X. P., Hu, S. H., Zhu, Y. W., & Pu, Q. S. (2022). Research on the escape mechanism and influencing factors of harmful gas induced by blasting excavation in deep rock tunnel. *Environmental Earth Sciences, 81*(18).

Qiu, P., Su, P. D., Li, Y. G., Lu, X. H., Chen, W. Y., Ahmed, M. S., Gentzis, T., & Mansour, A. (2025). Formation processes, accumulation patterns and risk mitigation strategies for harmful gases in tunnels within the complex geological structure area of Southwest China. *Bulletin of Engineering Geology and the Environment, 84*(6).

Shahin, H. M., Nakai, T., Ishii, K., Iwata, T., & Kuroi, S. (2016). Investigation of influence of tunneling on existing building and tunnel: Model tests and numerical simulations. *Acta Geotechnica, 11*(3), 679–692.

Stefánsson, A. (2017). Gas chemistry of Icelandic thermal fluids. *Journal of Volcanology and Geothermal Research, 346*, 81–94.

Sun, Q. H., Liu, X., Bao, Y. H., De Corte, W., & Taerwe, L. (2025). Experimental study on the leakage-induced structural collapse of segmental tunnels. *Underground Space, 24*, 22–43.

Sun, S. B., Yan, S. H., Cao, X. P., & Zhang, W. (2023). Distribution law of the initial temperature field in a railway tunnel with high rock temperature: A model test and numerical analysis. *Applied Sciences-Basel, 13*(3).

Surma, F., & Geraud, Y. (2003). Porosity and thermal conductivity of the Soultz-sous-Forets granite. *Pure and Applied Geophysics, 160*(5–6), 1125–1136.

Tang, Z. Q., Gao, K., Tao, C. F., Liu, Y. J., & Qi, Z. P. (2024). The influence of tunnel aspect ratio on the gas temperature distribution in advancing tunnel. *Tunnelling and Underground Space Technology, 149*, 105818.

Torno, S., & Toraño, J. (2023). Methane emission outbursts in the mine face of two galleries: Computational fluid dynamics analysis and on-site calibration. *Energies, 16*(21).

Tu, S. Q., Li, W., Zhang, C. P., Wang, L. B., Jin, Z. X., & Wang, S. X. (2024). Seepage effect on progressive failure of shield tunnel face in granular soils by coupled continuum-discrete method. *Computers and Geotechnics, 166*.

Wang, C. Y., Zhang, D. M., Tan, D. J., Ye, J. H., Wang, X. L., Wang, C. Y., & Li, Q. L. (2024). Study on the evolution of limestone damage and permeability under the tunnel driving stress path. *Construction and Building Materials*, 425.

Watanabe, Y., Yokoyama, S., Shimbashi, M., Yamamoto, Y., & Goto, T. (2023). Saturated hydraulic conductivity of compacted bentonite-sand

mixtures before and after gas migration in artificial seawater. *Journal of Rock Mechanics and Geotechnical Engineering, 15*(1), 216–226.

Xu, G. A., Jing, H. W., & Qiu, Y. (2019). Development and application of a test system for modeling tunnel excavation with transparent rock surrogate. *Geotechnical Testing Journal, 42*(3), 638–655.

Yuan, C. L., Xian, X. H., & Chai, X. Q. (2022). Study on comprehensive disaster control mode of coal and gas (CO2) outburst and steep coal steam. *China Coal, 48*(S2), 180–186 (in Chinese).

Zhang, F. S., He, G. P., An, M. K., Huang, R., & Elsworth, D. (2025). Permeability evolution of fluid-injection-reactivated granite fractures of contrasting roughnesses. *Underground Space, 20*, 33–45.

Zhang, H. Y., Chen, L., Liu, J., Wang, C. P., Ma, L. K., & Wang, W. (2023). Effect of stress induced damage on gas permeability of Beishan granite. *European Journal of Environmental and Civil Engineering, 27*(8), 2717–2730.

Zhao, C. X., Lei, Q. H., & Zhang, Z. X. (2025). Impact of fracture networks on the structural deformation of lined rock caverns under high internal gas pressure. *Underground Space, 21*, 252–269.

Zhou, Y. F., Li, C. F., & Song, G. M. (2016). Discussion on control measures for H2S in Yuelongmen Tunnel on Chengdu-Lanzhou Railway. *Tunnelling and Construction, 36*(10), 1251–1257 (in Chinese).

Zhu, C. F., & Cai, S. (2020). Study on borehole arrangement methods for gas extraction by hydraulic slotting in long-distance through-coal seam tunnel. *Geofluids*, *2020*.

Zhu, G. Y., Zhang, S. C., & Liang, Y. B. (2007). The controlling factors and distribution prediction of H_2S formation in marine carbonate gas reservoir, China. *Chinese Science Bulletin, 52*, 150–163.